Department of Precision and Microsystems Engineering

Characterization of biosensing with integrated photonic microchips for wearable photonics in health monitoring

Haotian Hu

Report no : 2023.067

Professor : Dr. G. J. Verbiest, Dr. W. J. Westerveld Specialisation : Dynamics of Micro and Nanosystems

Type of report : MSc thesis
Date : 24 August 2023



Characterization of biosensing with integrated photonic microchips for wearable photonics in health monitoring

Ву

Haotian Hu

in partial fulfilment of the requirements for the degree of

Master of Science in Mechanical Engineering

at the Delft University of Technology, to be defended publicly on Thursday August 24, 2023 at 9:30 AM.

Supervisor: Dr. G. J. Verbiest

Dr. W. J. Westerveld

Thesis committee: Dr. M. K. Ghatkesar TU Delft

This thesis is confidential and cannot be made public until August 24, 2025.

An electronic version of this thesis is available at http://repository.tudelft.nl/.



Abstract

Photonics biosensors convert biomolecular interactions into quantifiable optical signals for biomedical analysis, which enable continuous monitoring of health indicators. Among them the microring resonator has a good sensing performance and a very broad application prospect. This thesis studies sensing with microfluidic integrated microring resonator photonic microchips.

This thesis adopts finite element method to simulate the optical behavior of waveguides and reactions in the microfluidic channel. The microfluidic channel was designed and prepared and then integrated to the photonic chip. The optical performance parameters of the micro ring resonator were tested by using a high-precision optical test system, and the Q factor can reach the value of more than 21000. The sensing performance of waveguide microring was studied using the concentration of sodium chloride and glucose solution as the detection object. By monitoring and analyzing the resonance wavelength shift of microring at different concentrations, the detection sensitivity and detection limit of the sensing chip were determined, which are 53.3 nm/RIU and 3.752×10^{-6} RIU respectively. The feasibility and effectiveness of the optical waveguide chip sensing have been verified.

Acknowledgements

I would like to express my appreciation to my supervisors Dr. Gerard Verbiest and Dr. Wouter Westerveld for the continuous support and guidance throughout the research process.

I would like to thank Tufan Erdoğan for the discussions and support on configuring test bench.

Furthermore, I would like to thank Dr. Satadal Dutta, Sifeng He, Huaiyang Liu and all the lab mates for their assistance during the research process.

Contents

Abstract	i
Acknowledgements	ii
1 Introduction	1
1.1 Photonics MRR biosensors	2
1.1.1 Microring resonators	2
1.1.2 Sensing principle of microring resonators	4
1.1.3 Advantages of MRR biosensors	5
1.2 Microfluidics	5
1.3 State-of-the-art MRR biosensors	6
1.4 Objectives of the research and thesis organization	8
2 Theoretical bases and simulations of MRR biosensor	10
2.1 Performance parameters of MRRs	10
2.1.1 MRRs resonant equation	10
2.1.2 Radius-wavelength dispersion equation	10
2.1.3 Performance parameters	11
2.2 Sensitivity and limit of detection	12
2.3 Simulations of biosensing	13
3 Measurement platform for microfluidics integrated photonics chip	17
3.1 Development of microfluidics system	17
3.1.1 Design of the microfluidic chip	17
3.1.2 Preparation of microfluidic channel	23
3.2 Optical measurement system	25
4 Characterization of the photonics chip	28
4.1 Performance characterization of micro ring resonators	28
4.1.1 Characteristic parameters	28
4.1.2 Sensitivity and limit of detection	29
4.2 Biosensing characterization	35
4.3 Summary and discussions	38
5 Conclusions and outlook	40
References	41
Appendix	$\Delta\Delta$

1 Introduction

The development of sensitive, fast, cheap, simple and portable biosensors is a hot demand in the field of health monitoring. Such biosensors are divided into photonics, electromechanical and electrochemical biosensors [1, 2]. Among them, photonic biosensors have developed rapidly and received extensive attention for the advantage of strong anti-electromagnetic interference ability, high sensitivity and strong devices integration possibility [3, 4]. Photonic biosensors adopt a variety of optical devices to convert biomolecular interactions into quantifiable optical signals for biomedical analysis [5, 6]. Among them label free biosensor received much attention and after decades of research, many photonic biosensors with practical application value have been developed [3]. The label free biosensors especially show the great advantage of direct and real-time detection of bio-analytes because the analyte does not require any specific labeling and multi-step detection protocols that are required by label assisted sensing [7]. The current common photonic biosensors include surface plasmon resonance(SPR) biosensors, Mach-Zehnder interferometer(MZI) biosensors, and micro ring resonator(MRR) biosensors [8-11], as shown in Figure 1.

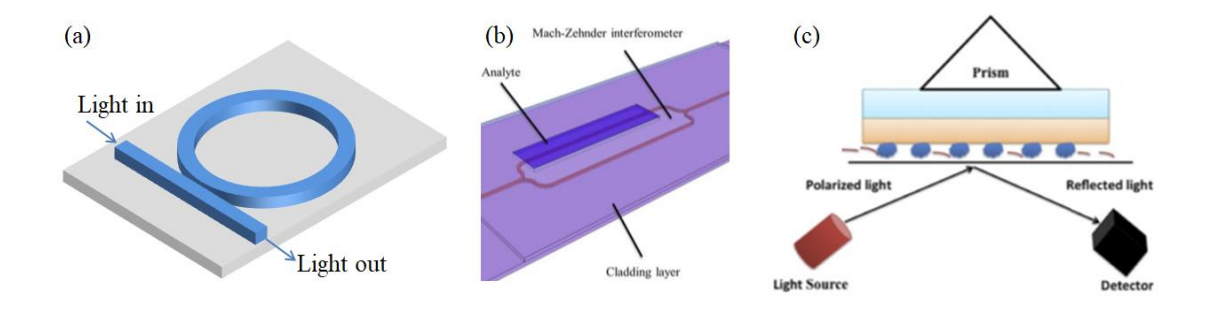


Figure 1 Photonic biosensors based on: (a) MRR, (b) MZI[10], (c)SPR[11].

Label free optical biosensing has been widely studied and their applications include protein detection, cell detection, DNA detection, biomolecular structure detection, and kinetic study of biomolecular binding interactions [12, 13]. These research results show the advantages of optical label free sensors that they are portable, able to resist external interference (such as electromagnetic noise), and sensitive on detection of bio-analytes. Therefore, the photonic biosensor has a good prospect in detection of bio-analytes for health monitoring.

1.1 Photonics MRR biosensors

The MRR biosensor is a kind of planar photonics waveguide based biosensor. This section introduces the structure, the sensing principle and the advantages of MRR biosensors.

1.1.1 Microring resonators

The basic structure of a silicon-on-insulator (SOI) waveguide, as illustrated in Figure 2, consists of two layers of materials. The core layer is made of silicon (Si), while the cladding layer is made of silicon dioxide (SiO₂), with refractive indices of 3.45 and 1.44, respectively. Due to the significant refractive index difference ($\Delta n = 2.01$) between Si and SiO₂, the Si waveguide imposes substantial constraints on the optical field, allowing light to propagate in small bending radius photon channels with negligible radiation loss[14]. Such waveguides exhibit high sensitivity, small bending radius, and compatibility with CMOS processes [15].

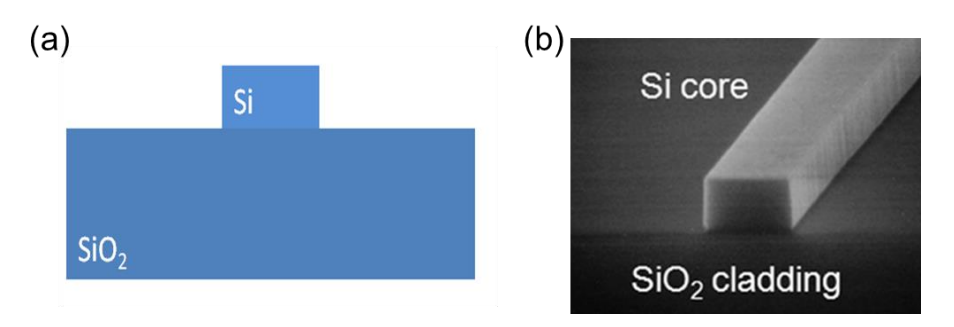


Figure 2 (a) Waveguide cross section shape profile (b) SOI waveguide photo [16]

When the light propagation is confined in the Si waveguides with total internal reflections on the interfaces, the evanescent wave will be generated, with the amplitude decays exponentially as the increasing of distance from the interface [17], as shown in Figure 3(a). The evanescent field plays an important role in MRR sensors since the MRRs operate based on the evanescent coupling of the light from the bus waveguide to the circular waveguide, as shown in Figure 3(b).

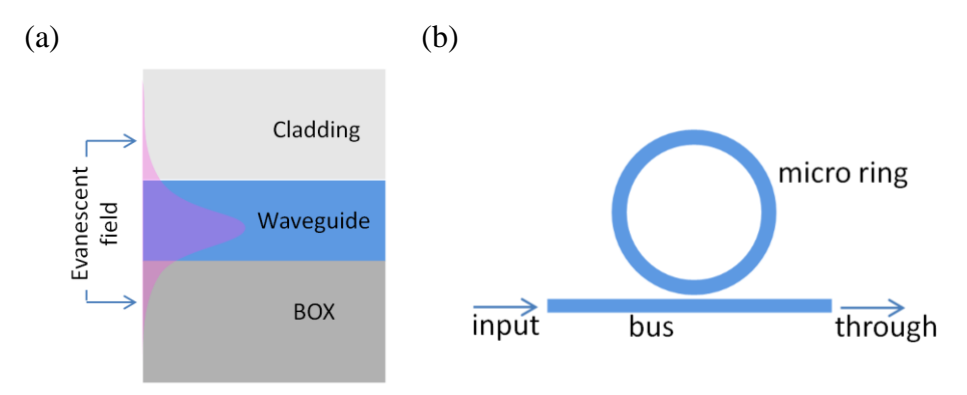


Figure 3 (a)Evanescent field of a SOI waveguide with upper-cladding and buried oxide (BOX), (b)Micro ring resonator schematic view

Due to the coupling between bus waveguide and ring resonator, a portion of the light will be coupled into the micro ring resonator when the light passing through the bus waveguide[8]. For the light with certain wavelengths, the phase of the light after one complete round trip in the ring will be in phase with the incoming light and the light circulating in the ring [9]. Such wavelengths are known as resonances, which are determined by the circumference of the ring and the effective refractive index of the waveguide [18].

Therefore, when the light sweeps over a range of wavelengths, constructive interferences occur because of evanescent coupling and dips periodically occur on the spectrum. These dips represent phase-matched resonance wavelengths with light in the bus waveguide as shown in Figure 4.

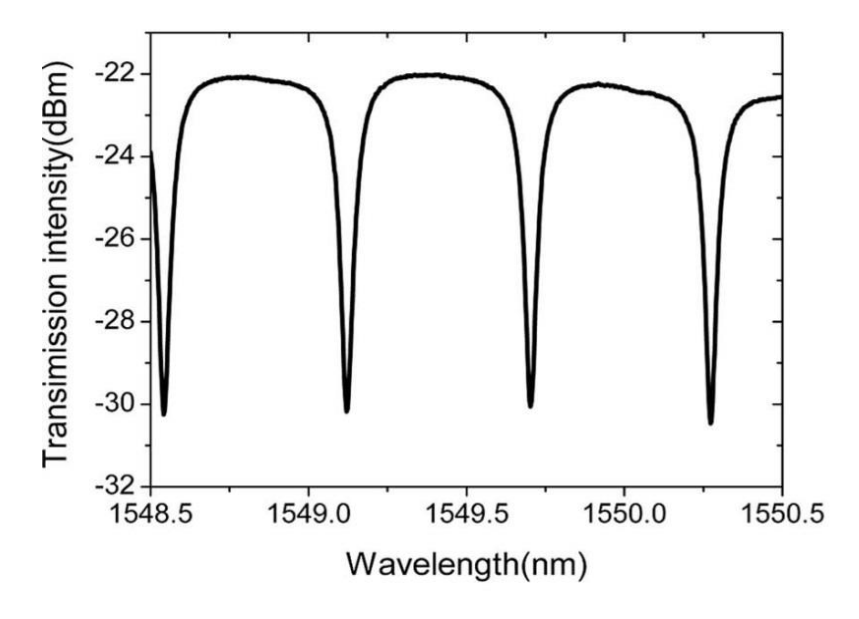


Figure 4 A measured optical transmission spectrum of microring resonator[19]

When the environment surrounding a micro ring resonator waveguide undergoes changes, it leads to a variation in the effective refractive index of the waveguide, resulting in a shift in the resonant wavelength. Hence, when the ring is surrounded by the sample under test the information about the measured sample can be detected by monitoring the shift in the resonant wavelength.

1.1.2 Sensing principle of microring resonators

Micro ring resonator sensor can work as a refractive index detector based on evanescent wave. The change of the refractive index of the measured material leads to the change of the effective refractive index of the micro ring waveguide. This then leads to the change in resonance wavelengths. According to different sensing mechanisms, it is divided into homogeneous (bulk) sensing and surface sensing, as shown in Figure 5.

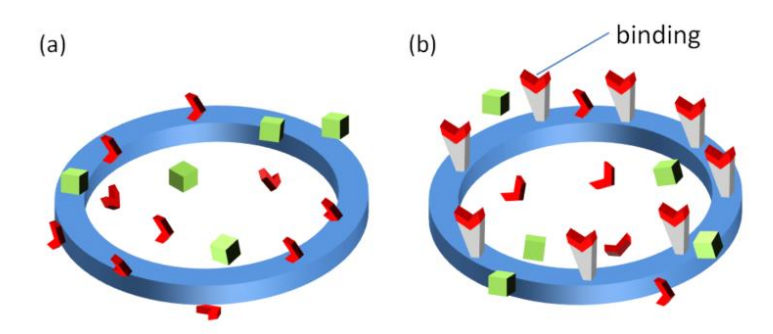


Figure 5 Sensing mechanisms: (a) Homogeneous sensing, (b) Surface sensing

Homogeneous sensing can only detect the change of concentration or refractive index of the whole solution instead of specific substances. For surface sensing, a chemically treated functionalized layer is added on the waveguide [20], so that the measured analyte is adsorbed to the waveguide surface, in which local refractive index is changed. The local refractive index change can cause a change in the effective refractive index of the waveguide, leading to a shift of the resonant wavelength. Therefore, the information of the measured sample can be detected by detecting the shift of the resonant wavelength, as shown in Figure 6.

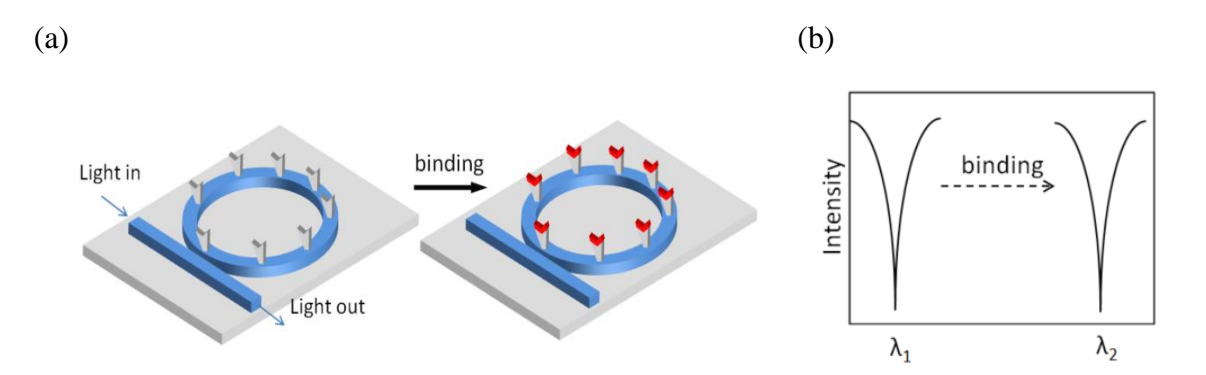


Figure 6 Schematic diagram of MRR surface biosensing and corresponding spectrum

1.1.3 Advantages of MRR biosensors

From the discussion in the previous sections, it is concluded that the optical waveguide micro ring biosensors have such advances:

Firstly, it enables label-free detection, resulting in low testing costs and enabling real-time on-site monitoring; the device has a small size and requires a small volume of test sample, which is portable and low-cost.

Secondly, the manufacturing process of waveguide structures is well-established and the preparation cost is low.

And finally, the micro ring structure is easily adaptable for array integration and suitable to be integrated with the microfluidics channel, enabling the construction of multiplexed biosensor which can achieve one-step measurement of multiple parameters.

1.2 Microfluidics

Because of the high sensitivity of micro ring resonator, the output spectral lines are easily affected by external factors such as vibration, dust and impurities. Meanwhile, to investigate photonics chip behaviors under different biomarker solutions, it is an important technology to smoothly control the solution with certain biological activity to flow through the chip surface so as to conduct multiplexed sensing. The microfluidic chip is the most common method to deal with small volume liquid detection[21]. Microfluidic chip refers to a miniaturized, integrated and automated experimental platform built on a few square centimeters or even smaller chips. Microfluidic chips generally manipulate fluid in micro scale to realize the expected physical, chemical or biological reaction effects [22]. Polymer materials have become comprehensively adopted materials for microfluidic channels because of their simple fabrication process and low cost. Polydimethylsiloxane (PDMS) is a common material for manufacturing

microfluidic chips. PDMS is a polymer organic compound with good light transmission and biocompatibility. It can be well adhered to the silicon chip, and is widely used in the microfluidics of bio-micro system including photonics biosensors [21-24].

1.3 State-of-the-art MRR biosensors

The micro ring resonator label free biosensors have been widely studied and achievements have been made on design, simulations and experimental works. Carlborg et al. [25] developed a six-port integrated microfluidic chip and conducted multiplex sensing, deriving a real-time resonance wavelength change with the changing of cladding liquid concentration and further characterized the detection limit and sensitivity. Washburn et al. [26] characterized the binding of biomarkers to different functionalized surfaces and measured the optical response of the waveguide. Heideman et al.[27] developed a microfluidics integrated photonics chip and measured wavelength shift by manipulating the fluid. Wu et al. [28] performed real-time detection of human Immunoglobulin G (IgG) with MRR chip, and achieved a detection limit of 0.5 µg/ml. Choi et al. [29] demonstrated kinetics of protein reactions of a photonic crystal integrated microfluidic chip with five channels made by replica molding. Salleh et al. [30] performed label-free chemical sensing on mouse IgG with MRR chip and plasma-bonded microfluidic channel.

It is concluded that biosensing based on micro ring resonators are widely investigated, a brief overview of reported examples is shown in Table 1. Many lab-on-chip microfluidic devices for photonics biosensing were developed and reported, the strategies of fabrication and integration are listed in Table 2. It is deduced that PDMS is the commonly adopted material for microfluidic channels integration to photonics chips and normally to precisely manipulate the fluid syringe or peristaltic pumps are used to control the fluid flow. A few microfluidic devices packaged with micro photonics chips are shown in Figure 7. These devices adopt different strategies on integrating to the photonics chips and on channels design.

Table 1 A brief overview of MRR biosensing investigations

Resonator type	Bio-analyte	Detection limit	Ref
Single ring	Human IgG	0.5 μg/ml	[28]
Array of single rings	Human serum albumin	3.4 pg	[31]
Single ring	g Green fluorescent protein 0.1 mg/ml		[32]
Single ring	Prostate specific antigen 0.4 nM		[32]
Suspended single ring	Trastuzumab	100 nM	[33]
Array of single rings	Bacterial tmRNA	524 pM	[34]
Cascaded double-ring	Human IgG	7.1 μg/ml	[35]

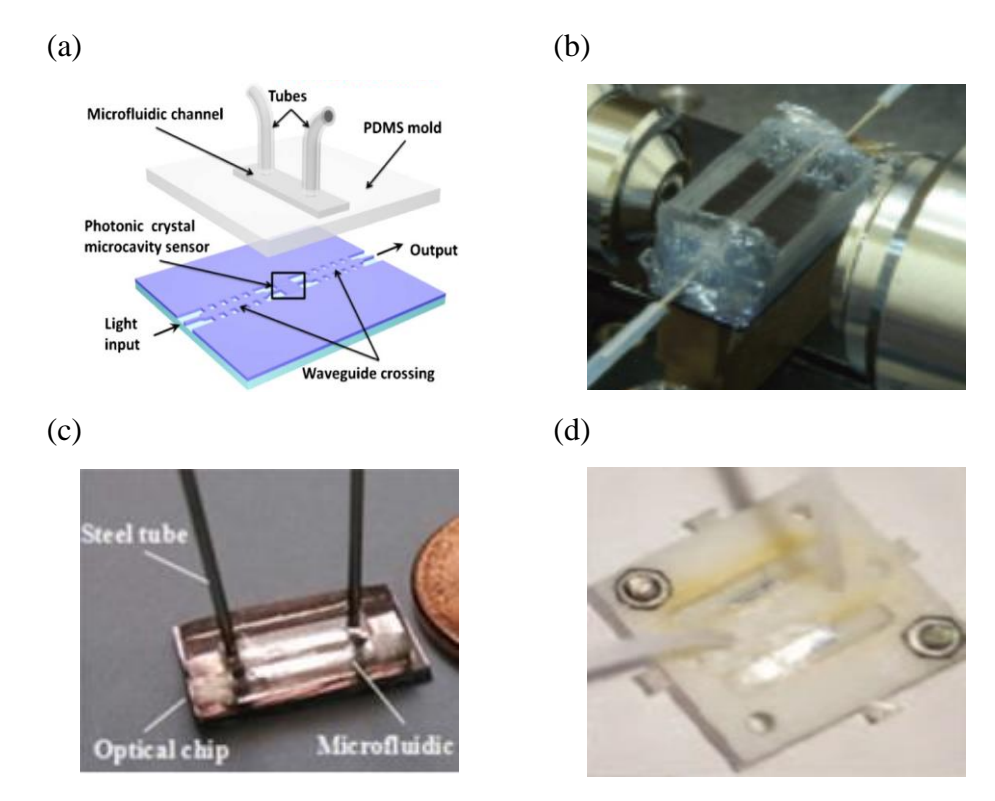


Figure 7 Microfluidics devices and packaging from literatures (a) Clamped PDMS chip[24], (b)Plasma-bonded PDMS chip[30], (c)Epoxy glued chip[35], (d)Plastic channel with PDMS seal[28]

Table 2 Microfluidics devices for photonics biosensing

Authors-Ref	Channel materials	Packaging method	Fluid control
Wang et al[24]	PDMS	Clamping	Syringe pump
Wu et al[28]	PDMS	Clamping	Peristaltic pump
Salleh et al[30]	PDMS	Plasma-bonding	Syringe pump
Chen et al[35]	PDMS	Epoxy glue	Syringe pump

1.4 Objectives of the research and thesis organization

The main objective of this thesis is to conduct a series of characterization based on SOI ring resonator photonic chips with microfluidic integration to test the performance of sensing. This requires the investigation of photonics chip optical response under different fluid environments, so as to characterize the performance characteristics of the chip such as sensitivity and limit of detection. The characterization system consists of multi-wavelength laser, optical fiber, grating couplers, biosensing chip, coupling waveguide, and optical power meter, as shown in Figure 8.

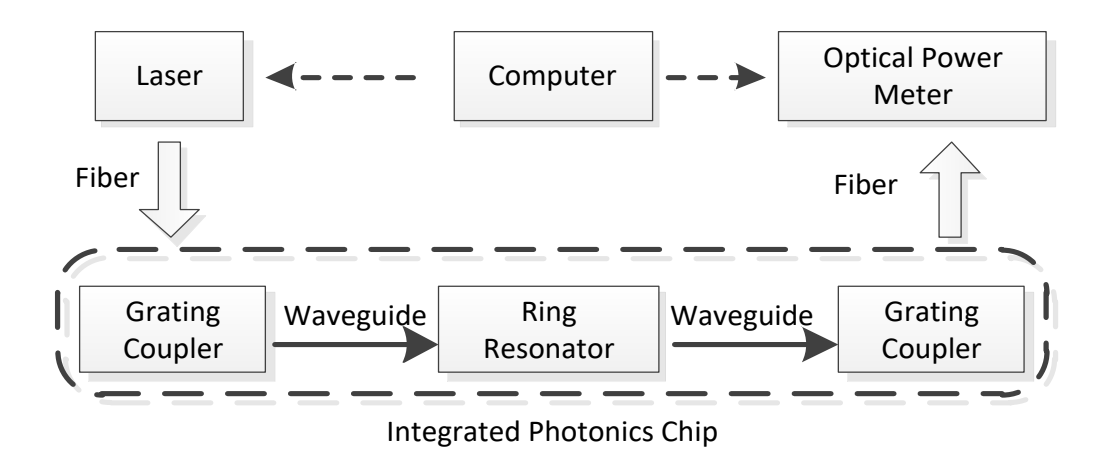


Figure 8 Schematic diagram of the characterization system

The main content of this thesis is divided into four parts: theoretical analysis, numerical simulation, construction of experimental setup, and sensing performance testing.

Chapter 2 first conducts a theoretical analysis of the micro ring resonator, introduces the theoretical model of the micro ring resonator, derives important characteristic parameters of the micro ring resonator, and finally conducts numerical simulation analysis of optical waveguide biosensing.

Chapter 3 mainly studies the measurement platform for microfluidic integrated photonics chip, designs and prepares microfluidic channels for materials, and studies the method of bonding microfluidic channels on waveguide chips. Then the high-precision optical testing system and testing process are presented.

Chapter 4 is the characterization of the photonics chip. The characteristic parameters of the micro ring are obtained from the transmission spectrum. The sensitivity and detection limit of the device to external refractive index changes are evaluated by solutions of different concentrations in microfluidic channel. The sensitivity to temperature changes was tested by controlling the chip temperature. And finally a biosensing demonstration is presented.

Chapter 5 presents the conclusions and outlook of the thesis.

2 Theoretical bases and simulations of MRR biosensor

This section includes performance parameters of MRRs based on photonics theories such as resonant equation, dispersion equation, free spectral range and quality factor, as well as performance parameters of biosensing such as sensitivity and limit of detection. Additionally, simulations of the waveguide under different sensing conditions are presented.

2.1 Performance parameters of MRRs

2.1.1 MRRs resonant equation

The MRR is frequency selective. Only the light with the optical length of the MRR that is an integral multiple of the wavelength can produce resonance and be strengthened, while the rest of the light will be gradually lost in the process of propagation. Its resonance equation is[36]:

$$2\pi R n_{eff} = m\lambda \tag{1}$$

In which, R is the radius of the microring, n_{eff} is the effective refractive index of the light wave propagating in the microring waveguide, λ is the optical wavelength in vacuum, and m is a positive integer.

2.1.2 Radius-wavelength dispersion equation

Only the light satisfying Equation (1) can propagate in the microring, but the effective refractive indices of different wavelengths in the waveguide are different, so the effective refractive index can be regarded as a function related to the wavelength, which yields,

$$2\pi R \frac{dn_{eff}}{d\lambda} + 2\pi n_{eff} \frac{\partial R}{\partial \lambda} = m \tag{2}$$

Then,

$$\frac{\partial R}{\partial \lambda} = \frac{m}{2\pi n_{eff}^2} \left| n_{eff} - \lambda \frac{dn_{eff}}{d\lambda} \right| \tag{3}$$

Therefore, it is obtained that the radius wavelength dispersion equation is,

$$\frac{\partial R}{\partial \lambda} = \frac{mn_g}{2\pi n_{eff}^2} \tag{4}$$

where n_g is the group refractive index of the waveguide,

$$n_{g} = n_{eff} - \lambda \frac{dn_{eff}}{d\lambda} \tag{5}$$

2.1.3 Performance parameters

The performance parameters of microring resonators mainly include the followings: resonant wavelength, free spectral range (FSR), full width at half maximum (FWHM) and quality factor Q.

Resonant wavelengths refer to the wavelengths that satisfy the resonance effect in a ring waveguide, leading to minimum transmissions in the coupled bus waveguide, which satisfy Equation(1):

$$\lambda_m = \frac{2\pi R n_{eff}}{m} \tag{6}$$

The free spectral range refers to the difference between two adjacent resonant wavelengths:

$$FSR = \lambda_{m+1} - \lambda_m \tag{7}$$

Differentiate Equation(1) on both sides:

$$2\pi R \frac{dn_{eff}}{d\lambda} \Delta \lambda_m = m\Delta \lambda_m + \lambda \Delta m \tag{8}$$

where, $\Delta \lambda_m$ is FSR and $\Delta m = -1$, combining Equation(1), there is:

$$FSR = \frac{\lambda^2}{2\pi R} \left(n_{eff} - \lambda \frac{dn_{eff}}{d\lambda} \right)^{-1}$$
 (9)

Rearranging based on Equation(5), it yields:

$$FSR = \frac{\lambda^2}{2\pi R n_a} \tag{10}$$

where n_g is the group index indicated in Equation(5).

From Equation(10) it can be seen that the free spectral range is inversely proportional to the ring radius, and the smaller the ring, the larger the free spectral range.

The full width at half maximum (FWHM) is defined as the difference between two wavelengths or frequencies centered on the resonant wavelength and corresponding to half of the maximum intensity, which can be intuitively displayed from the transmission spectrum.

The quality factor (Q factor) is defined as the ratio of the resonant wavelength to the

FWHM corresponding to the resonant wavelength:

$$Q = \frac{\lambda_{\rm m}}{FWHM} \tag{11}$$

The Q factor reflects the sharpness of the output spectrum, with a higher value indicating a sharper resonance peak and better wavelength selectivity of the micro-ring resonator.

2.2 Sensitivity and limit of detection

The sensing performance of MRRs can be characterized by the two parameters, detection sensitivity and limit of detection (LOD). The detection sensitivity is the change of the output signal (wavelength shift) compared with the input signal. According to Equation(1), when m and λ are fixed, the resonant wavelength will change with the change of $n_{\rm eff}$. By differentiating the two sides of Equation(1), it is derived that

$$m \cdot d\lambda = \left(\frac{dn_{eff}}{dt} \cdot dt + \frac{dn_{eff}}{d\lambda} \cdot d\lambda\right) \cdot 2\pi R \tag{12}$$

where $\frac{dn_{\rm eff}}{dt} \cdot dt$ represents the variation of waveguide refractive index and $\frac{dn_{\rm eff}}{d\lambda}$

represents the dispersion coefficient. Rearranging Equation(12), there is

$$d\lambda = \lambda \cdot \frac{\frac{dn_{eff}}{dt} \cdot dt}{\left(n_{eff} - \frac{dn_{eff}}{d\lambda} \cdot d\lambda\right)} = \lambda \cdot \frac{\frac{dn_{eff}}{dt} \cdot dt}{n_g} = \lambda \frac{dn_{eff}}{n_g}$$
(13)

Then,

$$\Delta \lambda = \frac{\Delta n_{\text{eff}}}{n_o} \lambda \tag{14}$$

where $\Delta\lambda$ is the resonant wavelength shift, $\Delta n_{\rm eff}$ is the effective index change of the waveguide and λ is the initial resonant wavelength before effective refractive index change.

Based on the sensing principles in section 2.2, the bulk sensitivity of the MRR can be expressed as the derivative of resonant wavelength over cladding refractive index:

$$S_{bulk} = \frac{\Delta \lambda}{\Delta n_{cladding}} \tag{15}$$

where, $\Delta\lambda$ is the magnitude of the resonant wavelength shift and $\Delta n_{cladding}$ is the

refractive index change of the bulk. Combining Equation(14), the equation can be rewritten as:

$$S_{bulk} = \frac{\Delta n_{\text{eff}}}{\Delta n_{cladding} n_g} \lambda. \tag{16}$$

Similarly, the surface sensitivity is then expressed as:

$$S_{surface} = \frac{\Delta \lambda}{\Delta t} \tag{17}$$

where, Δt is the thickness variation of the functionalized layer on the waveguide surface.

The LOD is the change of the minimum input signal that can be detected, which is related to detection sensitivity and wavelength resolution of optical read-out. The LOD is defined as:

$$LOD = \frac{\delta\lambda}{S} \tag{18}$$

where $\delta\lambda$ wavelength resolution of the detected spectrum at the output of test system and S is the detection sensitivity.

2.3 Simulations of biosensing

This section aims to conduct sensing simulations. Because the resonant wavelength shift of the ring resonator can be derived from the variation of the effective refractive index of the waveguide, the effective refractive indices of the silicon waveguide under different sensing conditions are simulated. The simulation results provide an insight into the sensing process and references for conducting the test.

The simulation of surface sensing is conducted in commercial software RSoft. A waveguide with width of 450nm and height of 220nm is modeled in RSoft CAD, as shown in Figure 9, with the cross section shown in Figure 10. The functionalized layer represents a layer of biomarker receptors and biomarkers on the top of the waveguide, with a variable thickness to simulate the optical performance with different amount of binding between biomarkers and receptors.

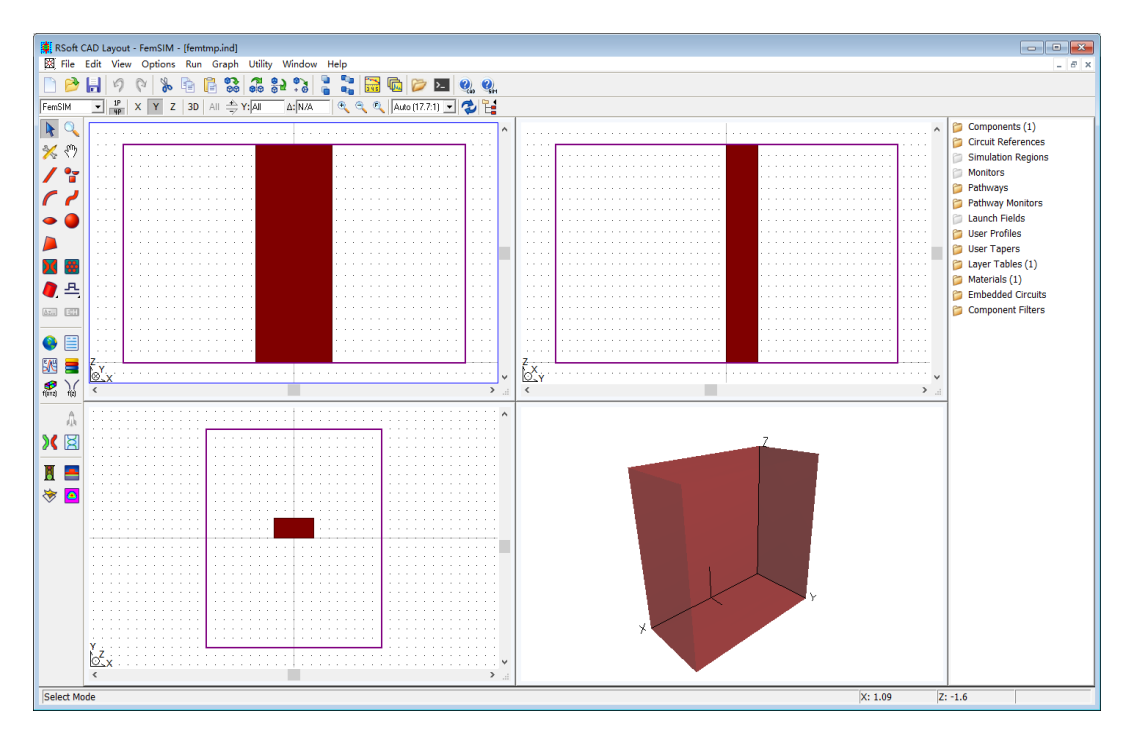


Figure 9 Waveguide modeled in simulation software RSoft

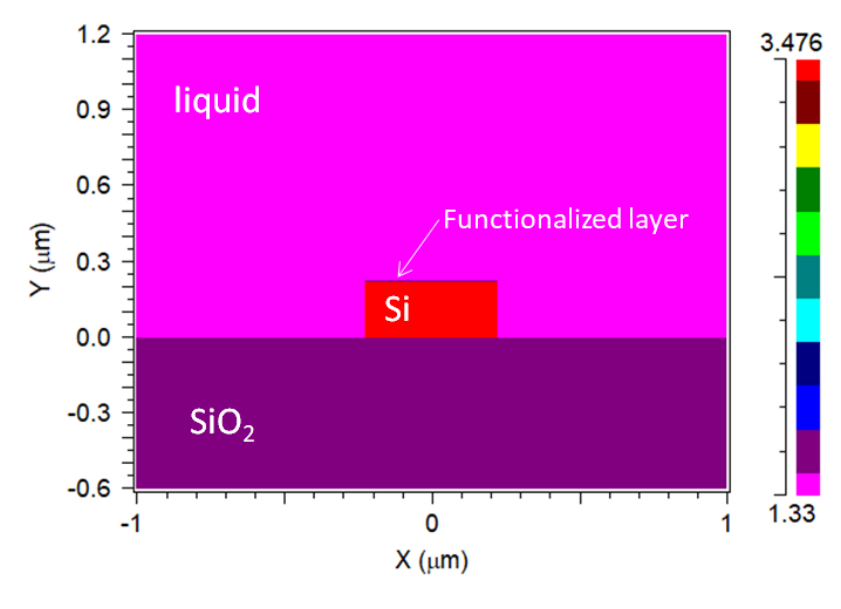


Figure 10 The cross section of modeled waveguide (Color bar: refractive index)

To simulate the optical response of surface sensing, finite element analysis is performed to compute the effective refractive indices of the waveguide under different functionalized layer thickness, where the thickness represents the amount of biomarkers bound to receptors. The chip functionalized layer with monolayer of biomarker receptors is set to 1.1nm thick and that with receptors monolayer and fully bound biomarkers is set to 7.4nm. The refractive index of the functionalized surface is 1.46. The simulation result is plotted in Figure 11. The slope of this curve gives the

effective refractive index sensitivity and it is calculated as 1.35×10⁻⁴ RIU/nm.

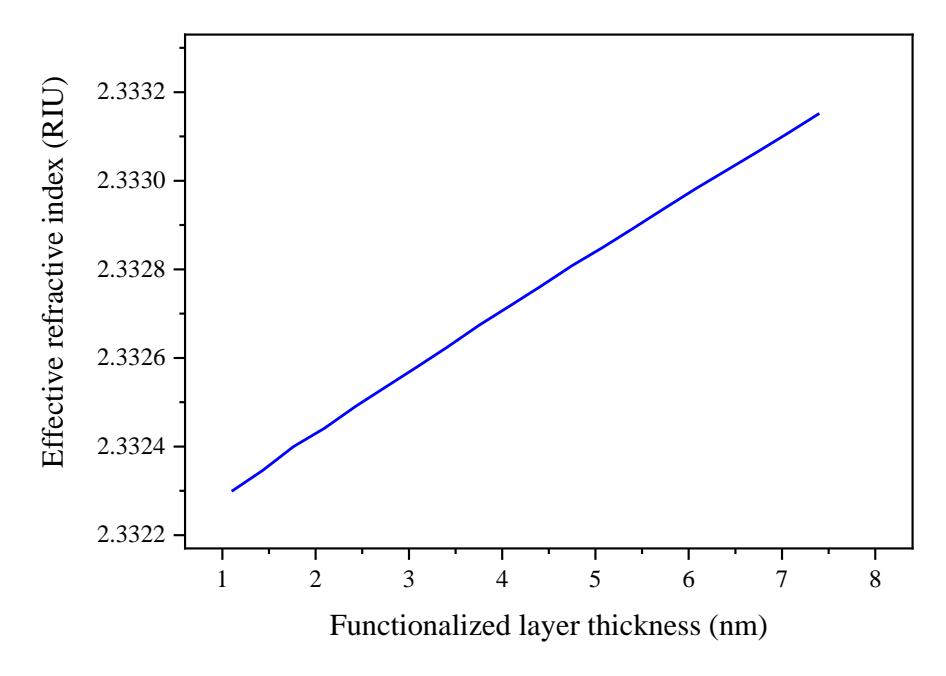


Figure 11 Surface sensing simulation results

The bulk sensing is simulated based on effective index change of the waveguide caused by cladding refractive index change. By sweeping the refractive index of the fluid cladding and computing the effective refractive index of the waveguide, the waveguide behavior and the sensing sensitivity is obtained. The effective refractive indices under different cladding's refractive indices are computed, as shown in Figure 12. The sensitivity is found as 0.156 RIU/RIU.

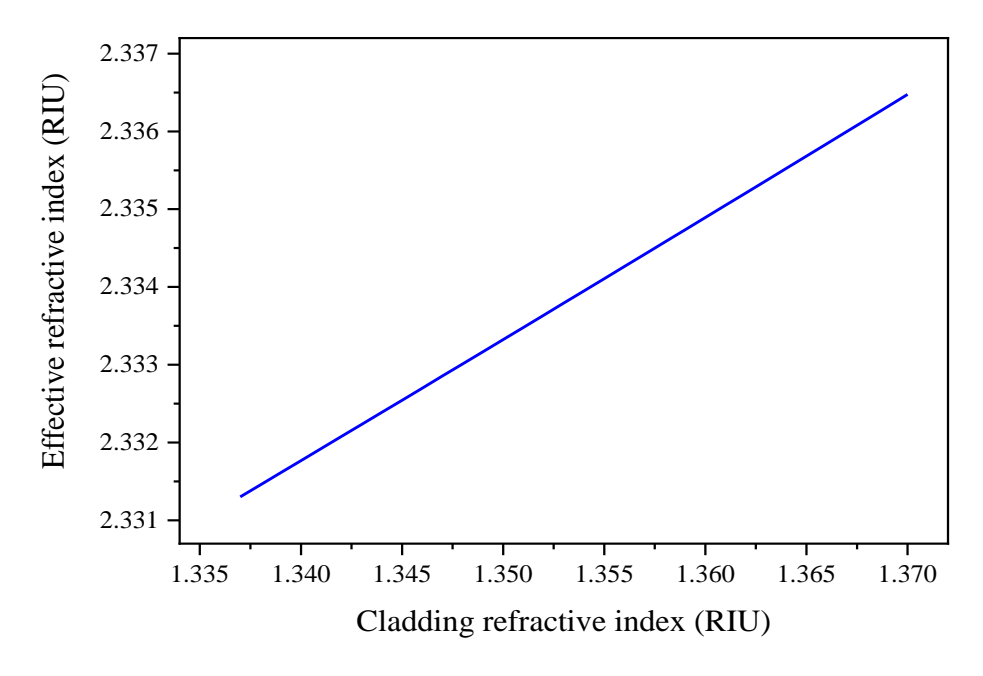


Figure 12 Bulk sensing simulation results

Then, the simulation of temperature sensitivity is performed. The increase in temperature will affect the resonance of the waveguide: due to the thermal expansion effect [36], the increase in temperature of the ring resonator leads to a change in device volume, which in turn causes the shift of resonant wavelength. On the other hand, due to the thermal optical effect, the refractive index of the material changes with temperature, resulting in a shift in the resonant wavelength. For silicon waveguide, because the thermo-optic coefficient $(1.86 \times 10^{-4} \text{ K}^{-1} \text{ [37]})$ is much larger than coefficient of thermal expansion $(2.55 \times 10^{-6} \text{ K}^{-1} \text{ [38]})$, the thermal expansion effect is neglected in the simulation. The simulation results of effective index change of waveguide with temperature changing are shown in Figure 13. The computed sensitivity is $1.885 \times 10^{-4} \text{ RIU}/^{\circ}\text{C}$.

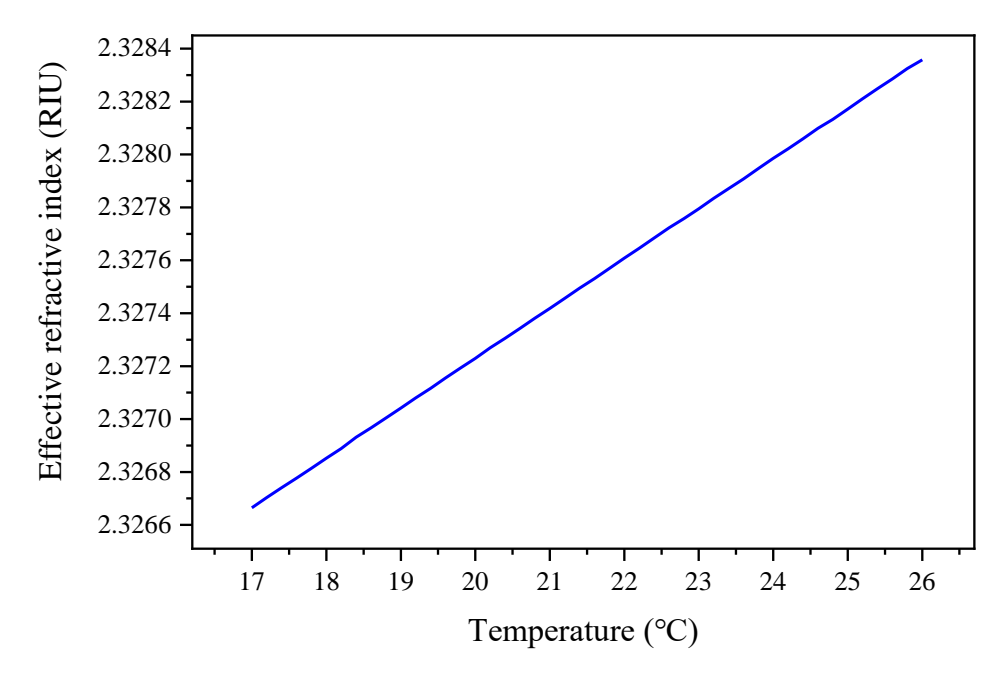


Figure 13 Effective index change of waveguide with temperature

After obtaining the effective index change of the waveguide, the resonant wavelength shift can be computed by Equation(14). Therefore, the resonant wavelength shifts under different sensing conditions are obtained and further the sensitivities of the resonance wavelength with respect to different sensing conditions are simulated.

3 Measurement platform for microfluidics integrated photonics chip

3.1 Development of microfluidics system

From section 1.2, it is concluded that stable manipulation of the fluid on the chip surface through microfluidic technology to ensure that the test solution can flow smoothly through the micro ring resonator is required for continuous measurement of spectral shift. Meanwhile, a well-designed micro channel can minimize the volume of test sample consumed for detection, and after detection, the device can be restored to a good state through simple cleaning work. Figure 14 shows the schematic diagrams of microfluidic system and microfluidic chip of the photonic chip.

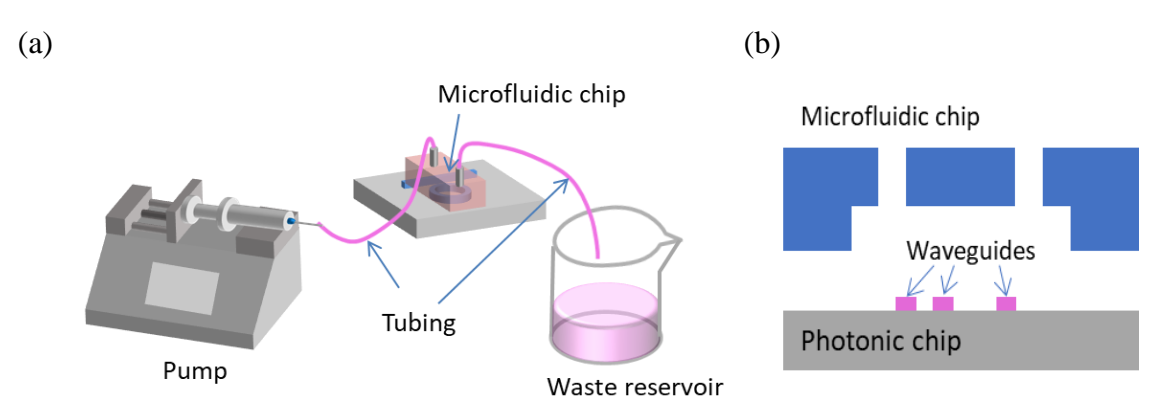


Figure 14 Microfluidics: (a) Microfluidic system, (b) Schematic of microfluidic channel

3.1.1 Design of the microfluidic chip

As discussed in chapter 1, the biosensing is based on surface adsorption of biomarkers to the micro ring. Due to the scale of micro-channels at the micrometer level, their flow characteristics are significantly different from macroscopic fluids, such as surface effects and scale effects. It is necessary to study the influence of the flow characteristics of fluids in the micro-channel on the surface adsorption of the micro ring in order to obtain stable and consistent surface coverage.

When a sample containing biomolecules flows over the functionalized surface, biomolecules will adsorb onto the surface. The adsorption is related to the nature and state of the adsorption surface, the concentration and nature of the adsorbed molecules, fluid flow rate, ambient temperature, pressure and other factors, and such adsorption is not a static state, but accompanied by the adsorption of free molecules and the desorption of adsorbed molecules in a dynamic process. When the adsorption and

desorption reach a dynamic equilibrium, there are a certain number of relatively stable adsorbed molecules on the surface, which is called equilibrium adsorption.

To design a microfluidic channel such that the bio-analytes can be uniformly attached to the waveguide, the influence of channel dimensions to the biomarker attaching quality should be investigated.

The mathematical formulation of the simulation mainly includes description of flow velocity, transport of species and reaction kinetics, respectively. The flow in microfluidic channel is described by a laminar flow model, for its low flow rate and micrometer scale channel, with the following governing equations:

$$\frac{\partial \rho}{\partial t} + \rho \nabla \cdot \vec{V} = 0 \tag{19}$$

$$\rho \left(\frac{\partial \vec{V}}{\partial t} + \vec{V} \cdot \nabla \vec{V} \right) = -\nabla P + \upsilon \nabla^2 \vec{V}$$
 (20)

where ρ is the density of fluid, \vec{v} is the flow velocity field, P is the pressure and v is the liquid viscosity.

The reaction kinetics is described by equilibrium equation of adsorbed molecules, which is expressed as[39]:

$$\frac{dC_s}{dt} = K_{ads} \cdot C_p \cdot \Theta - K_{des} \cdot C_s \tag{21}$$

where, K_{ads} is the association rate constant, K_{des} is the dissociation rate constant,

 Θ represents the receptors surface density and C_p C_s are biomarker concentration in solution and on surface respectively.

The species concentration field and transport of analytes is governed by [39]:

$$\frac{dC_p}{dt} + \nabla \left(-D_p \cdot \nabla C_p \right) + \vec{V} \cdot \nabla C_p = 0 \tag{22}$$

where, D_p is diffusion coefficient of molecules in liquid.

The channel model of microfluidics is established by multiphysics simulation software COMSOL, as shown in Figure 15, in which fluid dynamics, species transport and reaction kinetics are simulated. Probes are set at the seven points marked in the figure to monitor fluid velocity and surface coverage under different parameters. Due to the symmetry of the channel and the ring, probing points are evenly distributed on half of the ring, in order to simplify the computation. Taking human epidermal growth factor receptor 2 (Her2) solutions as the simulation object, the relevant parameters adopted in computation are shown in Table 3

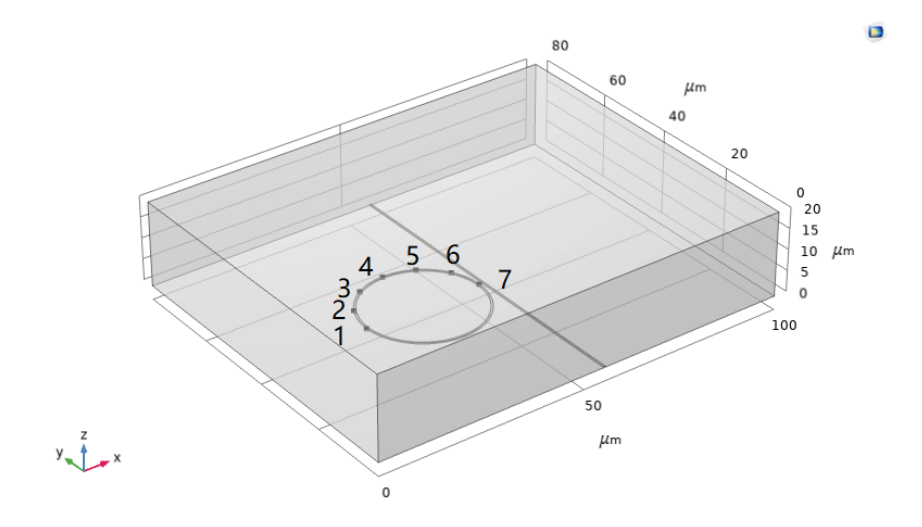


Figure 15 Microfluidic channel model

Table 3 Parameters utilized in simulation

Parameters	Value
Diffusion coefficient $D_p(m^2 \cdot s^{-1})$	3×10 ⁻⁹
Association rate constant K_{ads} ($M^{-1} \cdot s^{-1}$)	2.3×10^{5} [40]
Dissociation rate constant $K_{des}(s^{-1})$	6.8×10^{-3} [40]
Receptors surface density Θ ($mol \cdot m^{-2}$)	1×10^{-5}
Solution concentration $C_p(M)$	4.3×10^{-5}

At the entrance of the microchannel, the biomarker solution flows into the microchannel, and upon reaching the surface of the microring, some molecules are adsorbed on the surface of the microring. The surface coverage ratio increases, and then maintains a relatively stable value, as shown in Figure 16. Under the combined action of molecular adsorption and desorption, the molecular coverage reaches its maximum value and maintains equilibrium, where the equilibrium value is relevant to the geometry of the channel and the concentration of the biomarker solution.

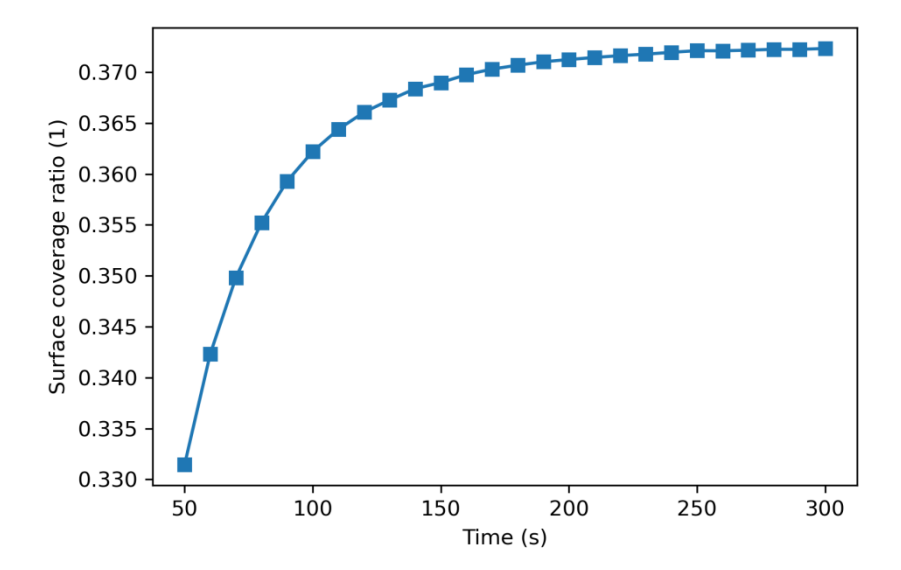


Figure 16 Changes in surface coverage of adsorbed molecules over time

From Equations (19)-(22), it is concluded that fluid velocity has a significant impact on molecular adsorption. The higher the fluid velocity, the lower the adsorption rates of molecules on the microring; and the higher the fluid velocity, the more nonuniform the molecular adsorption rate.

The fluid velocity field is influenced by the dimensions of the microfluidic channel, because of the scale effect and the non slip boundary conditions at the sidewall. In order to ensure that molecules in the fluid are evenly and as much as possible adsorbed on the surface of the microring, the micro channel structure should be reasonably designed and a reasonable fluid velocity should be set.

To investigate the effect of channel size on molecular adsorption, the standard deviation of the surface coverage rate at 7 points on the microring is used to represent the uniformity of molecular adsorption:

$$\sigma = \sqrt{\frac{1}{7} \sum_{i=1}^{7} \left(C_{Si} - \overline{C}_s \right)^2} \tag{23}$$

$$\overline{C_s} = \frac{1}{7} \sum_{i=1}^{7} C_{Si}$$
 (24)

where, C_{Si} is the surface coverage rate at each indicated probing point and $\overline{C_s}$ is the average of surface coverage rate values of all probing points.

The less the standard deviation, the more uniform the surface coverage. Figure 17 indicates the standard deviation on surface coverage of seven probing points under

different channel width.

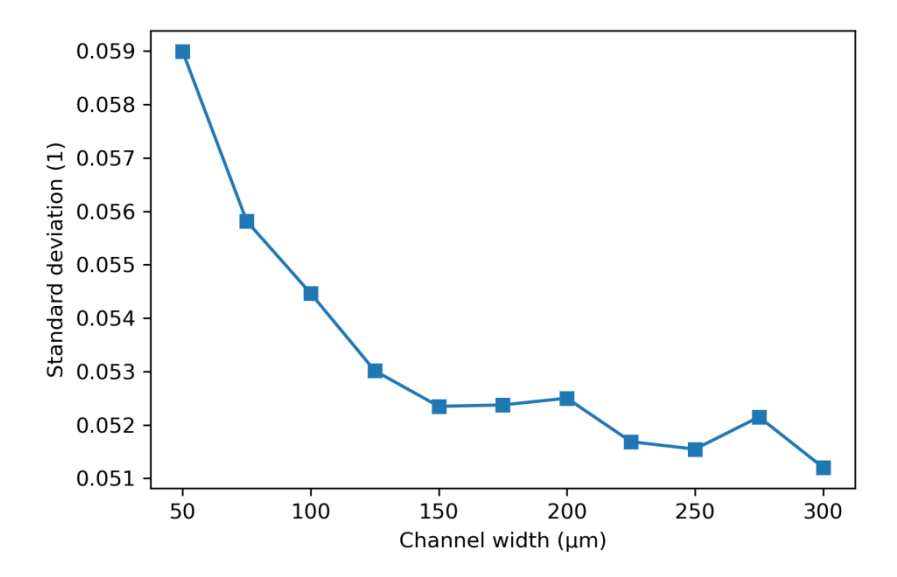


Figure 17 Variation of standard deviation of surface coverage with channel width

It can be seen that as the channel width increases, the standard deviation decreases, indicating that the larger the channel width, the more uniform the molecular adsorption. When the channel width increases to 175 μm , the standard deviation converges to a value around 0.052, indicating that increasing the width has no significant impact on the distribution of adsorbed molecules. Therefore, it can be considered that this width is a critical width to have a relative uniform distribution with the prescribed parameters. Figure 18 shows the distribution of surface coverage under different channel widths. It can be seen the surface coverage with 300 μm channel width is more uniform than that of 50 μm .

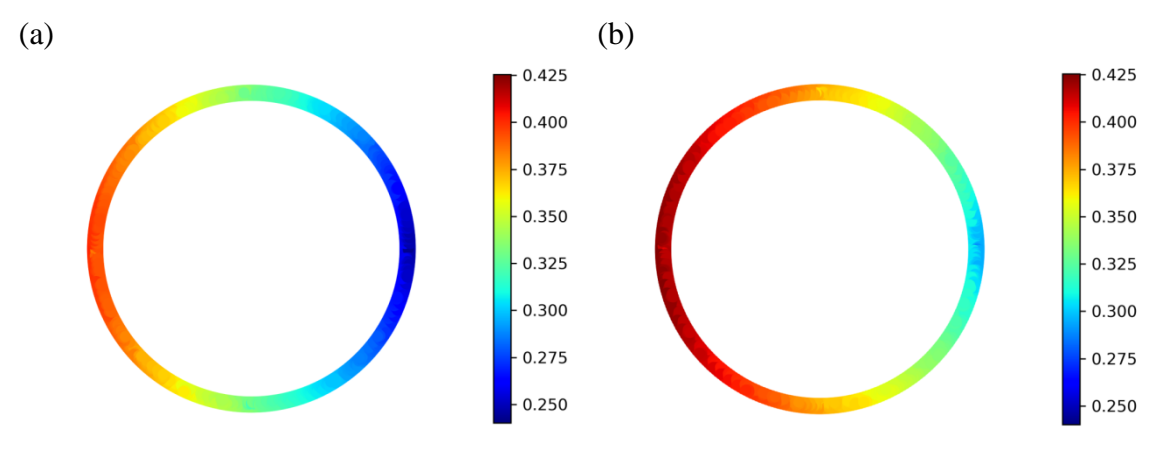


Figure 18 Surface coverage distributions under different channel widths: (a) 50 μm, (b) 300 μm

Similarly, the influence of channel height to the surface coverage uniformity is studied. The uniformity indicator (standard deviation) under different channel height is shown in Figure 19. The standard deviation of surface coverage values on the probing points converges to 0.04 when the channel height reaches 70 μ m. The surface coverage distributions under channel heights 10 μ m and 100 μ m are shown in Figure 20.

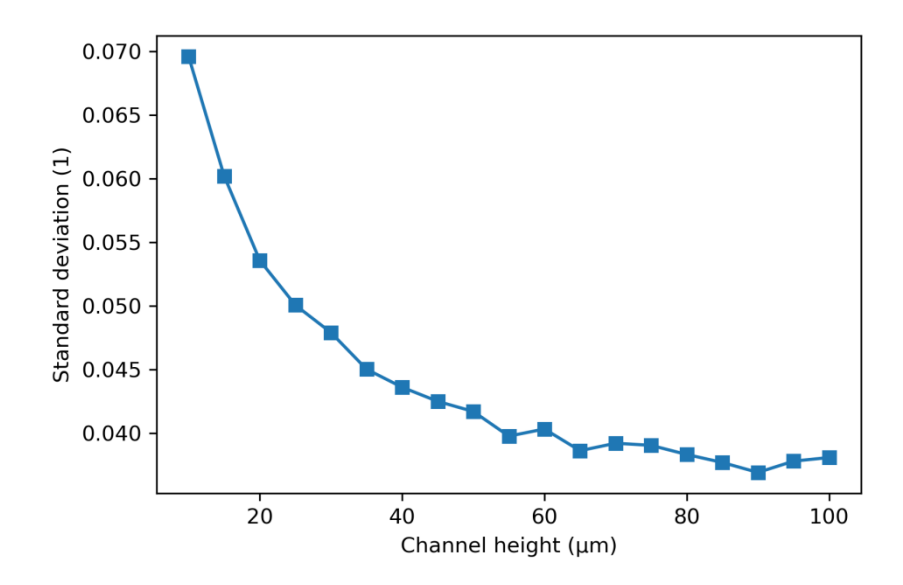


Figure 19 Variation of standard deviation of surface coverage at various points with channel height

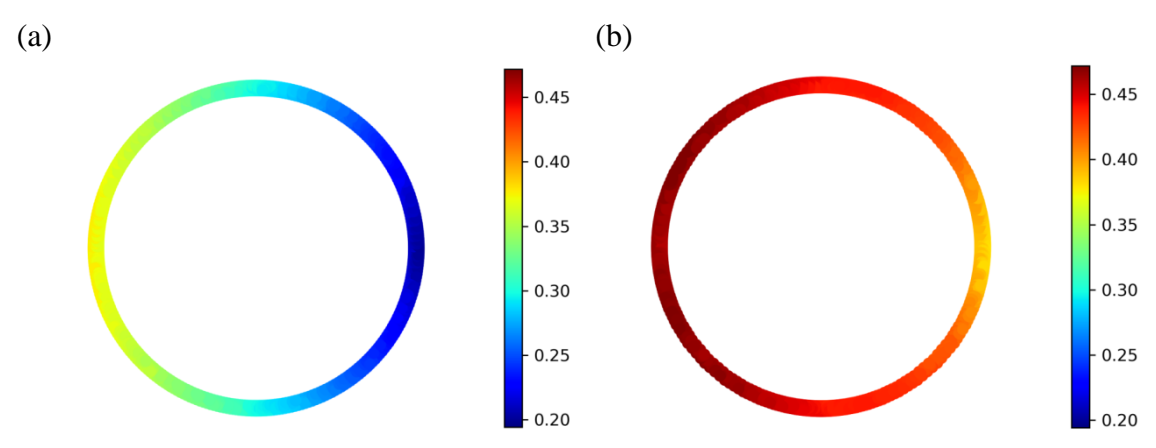


Figure 20 Surface coverage distributions under different channel heights: (a) 10 μm, (b) 100 μm

In summary, the larger the size of the micro channel, the more uniform the distribution of fluid velocity, which is more conducive to the adsorption of biomolecules on the surface of the microring. However, being too large in size is not conducive to miniaturization and integration of the device, and requires a larger

volume of test samples during operation. From the above analysis, it can be seen that for a radius of $14 \, \mu m$, height of $0.22 \, \mu m$ microring sensor, when the channel width is $175 \, \mu m$ and height is $70 \, \mu m$, it can meet the requirements of uniform molecular adsorption. Limited to the fabrication process and in order to easily align the channel with the microring resonator, the width of the channel is set to $1 \, mm$ and the height is set to $0.8 \, mm$. Since this channel size is larger than the critical value, a relative uniform biomarker distribution can be obtained.

3.1.2 Preparation of microfluidic channel

PDMS is selected as the material for microfluidic channel fabrication. It is a kind of polymer material, which is one of the widely used materials for microfluidics chip fabrication. The fabrication method of replica molding (REM) is adopted, for its process simplicity and efficiency. REM requires prefabrication of positive masters or molds, and commonly used methods include LIGA, dry etching of silicon, wet etching of silicon, and SU-8 photoresist lithography [41-44]. Due to the complexity and high cost of these methods, this thesis adopts the stereolithography (SLA) 3D printing method to fabricate the mold for replica molding.

The PDMS used in the experiment is Sylgard 184 silicone rubber (Dow Corning, US), which is composed of a certain ratio of prepolymer and initiator, with a ratio of 20:3. After the mixing, it is necessary to stir the mixture to make it evenly mixed, and a large number of bubbles will appear after stirring. Bubbles need to be removed to prevent them from remaining in the cured PDMS. The experiment adopted a vacuum desiccator for degassing. Then, the PDMS after vacuum degassing was used as the material to cast the microfluidic channel.

The specific procedure for PDMS micro channel fabrication is described as follows:

- (1) Design the mold with CAD software;
- (2) Print the mold with SLA 3D printer;
- (3) Mix the base elastomer and curing agent and place the mixture in a vacuum desiccator for degasification;
- (4) Pour the mixture onto the prepared mold;
- (5) Cure the PMDS at a certain temperature until the prepolymer is fully cured;
- (6) Peel off the cured PDMS material from the mold;
- (7) Cut the PDMS to desired size and punch the holes for fluid inlet and outlet with a puncher.

The schematic diagram of microfluidic channel fabrication process is shown in Figure 21.

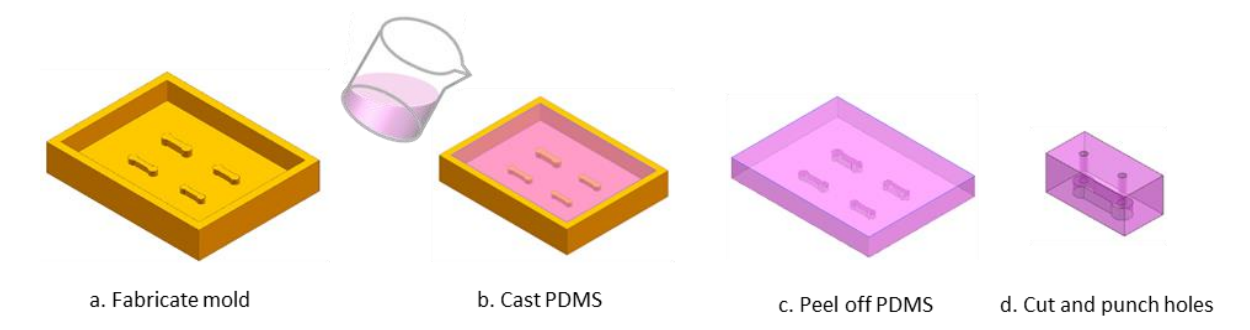


Figure 21 Microfluidic channel fabrication process

In the curing process, the curing of PDMS prepolymer might be inhibited, leading to incomplete curing and impeding reliable replication of channel structure. Sometimes PDMS may adhere to the mold, impeding the separation of PDMS and mold. This is because the resin monomers are not fully cured during the SLA 3D-printing[45]. The solution is to treat the SLA-printed mold with ultraviolet (UV) post-curing, solvents (ethanol, isopropanol) and high temperature; and coat the mold with a layer of hydrophobic material [45-47].

In the experiment the resin 3D printed mold was soaked in isopropanol for 30min followed by a treatment with UV post-curing under 100°C for an hour, to get rid of residual monomers as much as possible. The mold was then coated with a layer of polysiloxane to further prevent the residual monomers inhibit PDMS curing. The experimental results indicate that this method is effective. The fabricated mold and microfluidic channel are shown in Figure 22(a) and (b), respectively.

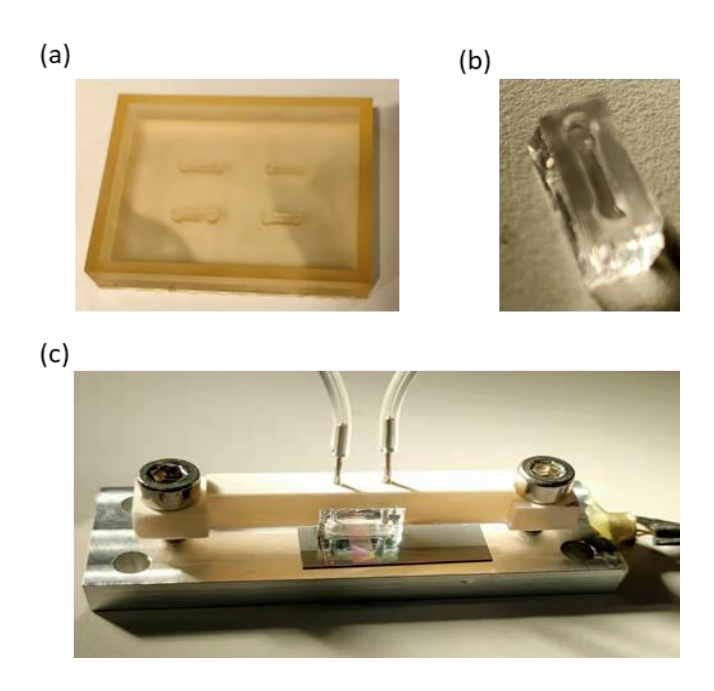


Figure 22 (a) Mold for casting, (b) PDMS channel, (c) Channel integrated with silicon chip by a fixture

The PDMS is then bonded to the silicon chip to create a microfluidic channel coupled with the microring. The commonly adopted techniques include surface activation to create chemical bonds between attached surfaces, attaching with adhesive and clamping the PDMS and silicon chip together with a fixture. Due to the first two options are irreversible bonding, the photonic chip will not be possible to separate. After repeated use, experimental drugs will inevitably remain on the surface of the chip, which cannot be thoroughly cleaned by flushing, resulting in inaccurate experimental results. Besides, the surface activation technique of plasma treatment and some of the adhesives have a negative influence on biological activity of biomarkers. Based on these reasons, a clamping fixture is adopted to bond the PDMS and silicon chip in this thesis. The PDMS channel and photonics chip are clamped with a resin fixture and a metal substrate, as show in Figure 22(c). Then, stainless steel needles are inserted into the microfluidic channel and connected to the microfluidic pump and waste reservoir with tubing, to create the entire microfluidics system. Thus the channel can be easily separated from and integrated to the silicon chip by mechanical fastening, so that the chip can be thoroughly cleaned with ultrasonic cleaner after each measurement.

3.2 Optical measurement system

The optical testing system is composed by laser input, optical reading, data acquisition, and microfluidics systems. The photo of the whole testing system is shown in Figure 23.

The system consists of the following instruments:

- 1 Tunable laser;
- 2 Polarization controller, controlling the polarization state of input light;
- 3 Input laser adjustment stage;
- 4 Chip holding stage, integrated with temperature transducer and Peltier element;
- **(5)** Microscopy camera;
- **6** Light source, providing light for camera observation;
- ① Output laser adjustment stage;
- Optical power meter;
- Oscilloscope;
- Syringe pump;
- (11) Temperature controller, with PID, accuracy 0.01°C;
- (12) Computer, controlling laser source and recording data from oscilloscope.

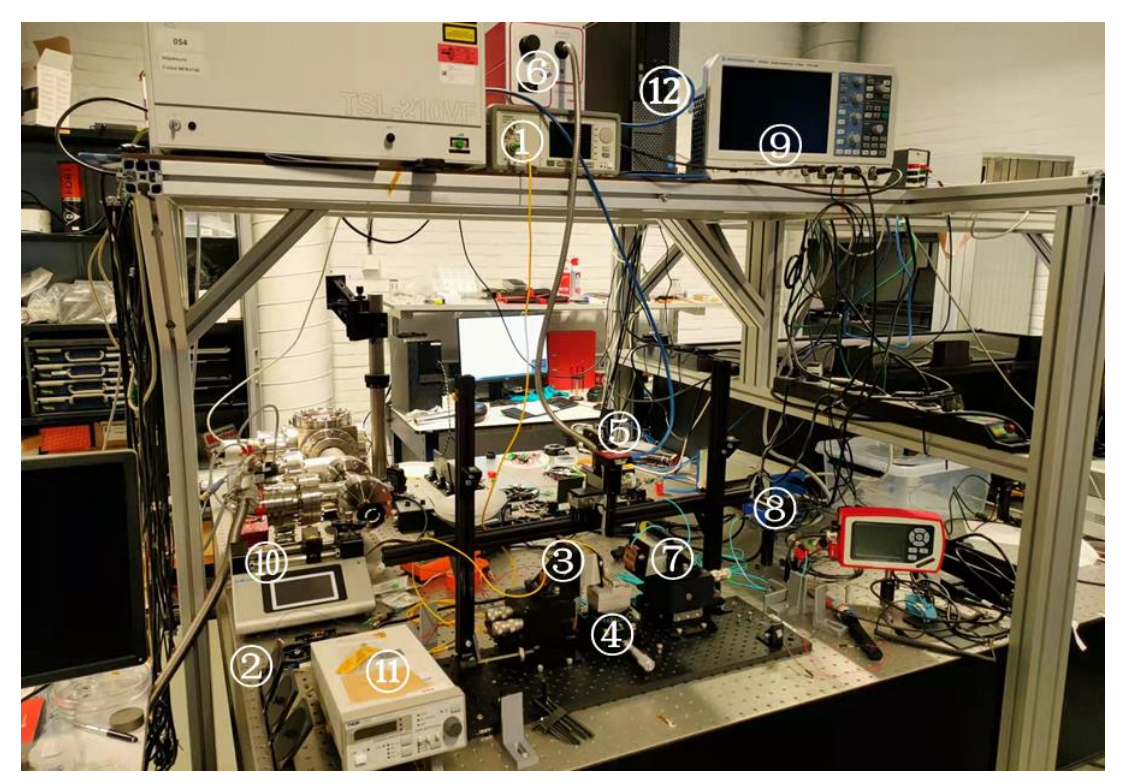


Figure 23 Photo of the optical measurement system

During the test, after being emitted by a tunable light source, light enters the micro ring resonator through an input fiber, undergoes a series of resonances, and enters the optical power meter through the output fiber. During the experiment, the chip is placed on an adjustable stage loaded with a temperature controller, which can accurately adjust the position and temperature of the chip. The input and out fibers are fixed on two 3-axis positioning stage, so as to align the fiber with grating couplers on the photonics chip.

Beam path of the test system is show in Figure 24.

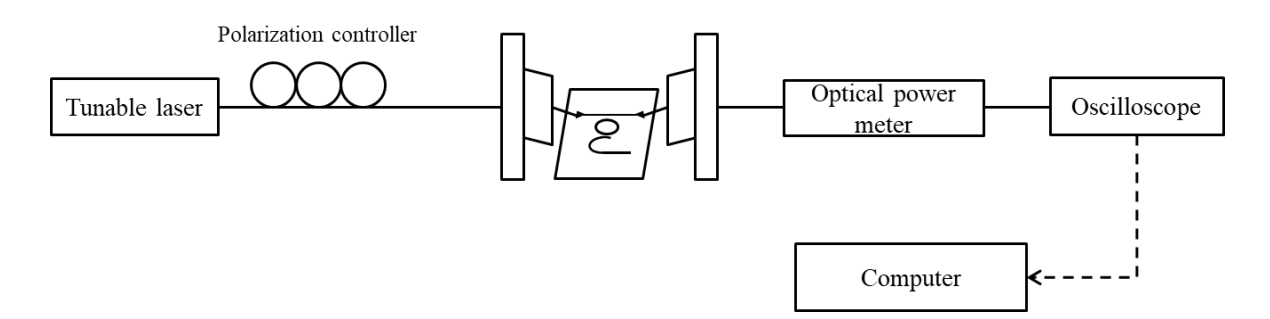


Figure 24 Beam path of the test system

The test procedures are as following:

- (1) Turn on the tunable laser and temperature controller, warming-up for 10 minutes;
- (2) Load the test chip to chip holding stage;
- (3) Adjust the position of the optical fiber and observe it through camera to align it with the grating coupler;
- (4) Active the laser and fine adjust the fibers and polarization controller to obtain a maximum output from optical power meter;
- (5) Use the computer program to control the instruments, sweep the laser wavelength and record the output power;
- (6) Adjust experimental variables (temperature, microfluidics);
- (7) Stop the computer program and save the data, then turn off instruments.

4 Characterization of the photonics chip

4.1 Performance characterization of micro ring resonators

4.1.1 Characteristic parameters

Before conducting sensing characterization experiments, in order to evaluate the performance of the micro ring resonator, the characteristic parameters of the micro ring resonator were measured. Transmission spectrum of the device was measured on the optical test bench, as shown in Figure 25 and Figure 26.

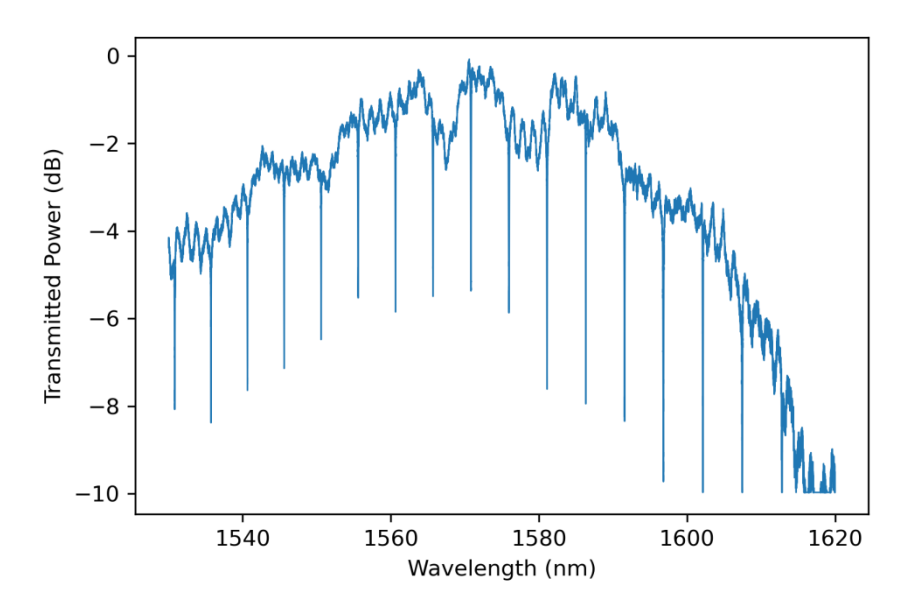


Figure 25 Microring resonator transmission spectrum

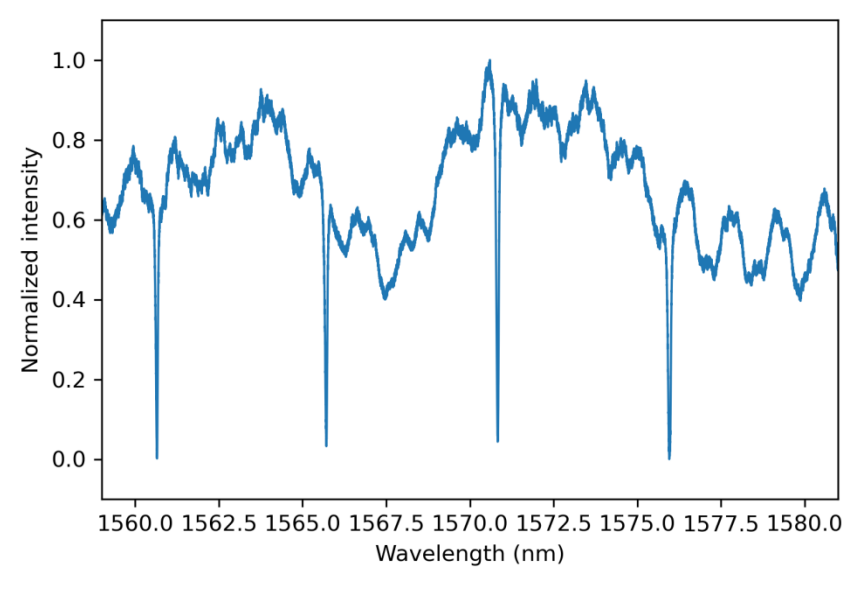


Figure 26 Microring resonator transmission spectrum from 1560nm to 1580nm

Based on the theoretical analysis in chapter 2, from the data shown in Figure 26 the characteristic parameters of the device (under water cladding) are derived. Free spectral range is 5.1 nm; full width at half maximum (FWHM) is 0.073 nm; and quality factor Q is 21512.2. These results imply that the microring resonator has a good optical performance for conducting sensing tests.

4.1.2 Sensitivity and limit of detection

After the performance of the device is examined, a series tests about sensitivity and limit of detection are conducted. The tests starts from temperature characterization followed by tests with NaCl, glucose and whey solutions as microfluidic environments.

To measure the sensitivity of the device to the temperature of the device, a temperature characterization test was conducted. During the test, water was continuously injected to the microfluidic channel, to provide a water cladding to the microring resonator. The transmission spectra were measured periodically, with tuning the temperature by temperature controller. Then, the resonant wavelength of each data recording time point was derived, and the resonant wavelength shift with time was computed. The transmission spectra under different temperatures are shown in Figure 27. The real-time detection of resonant wavelength shift is shown in Figure 28.

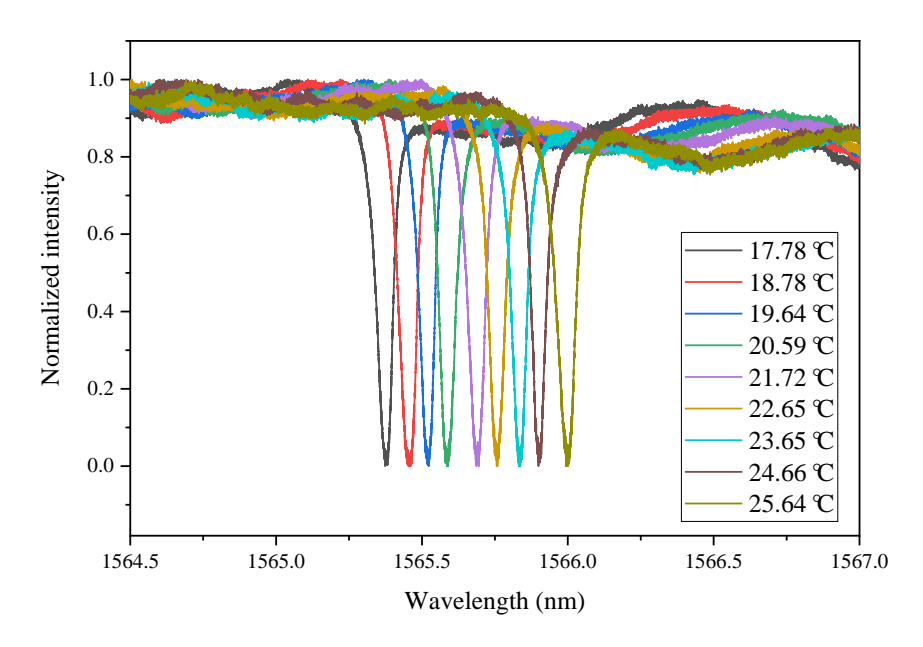


Figure 27 The spectra of microring resonances under different temperatures

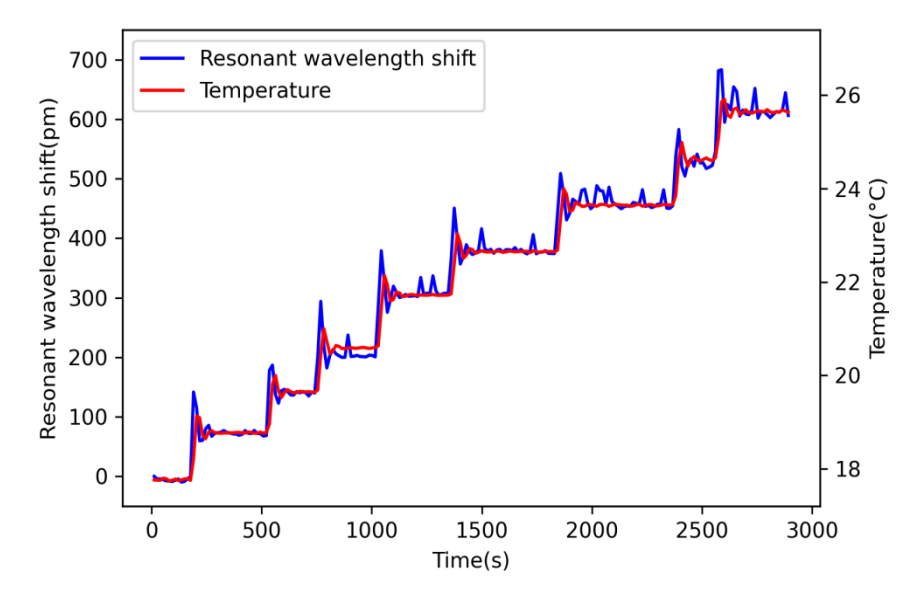


Figure 28 Real-time recording of resonance shift under temperature changing

The temperatures and corresponding resonant wavelength shifts are plotted in Figure 29, where the error bars are standard deviations of multiple measured data. The equation obtained after linear fitting is:

$$\Delta \lambda = 78.64T - 1397.61 \tag{25}$$

where $\Delta \lambda$ is the resonant wavelength shift and T is the temperature in Celsius. The coefficient of determination is 0.99975 in regression analysis, indicating a good linear relation between temperature and wavelength shift.

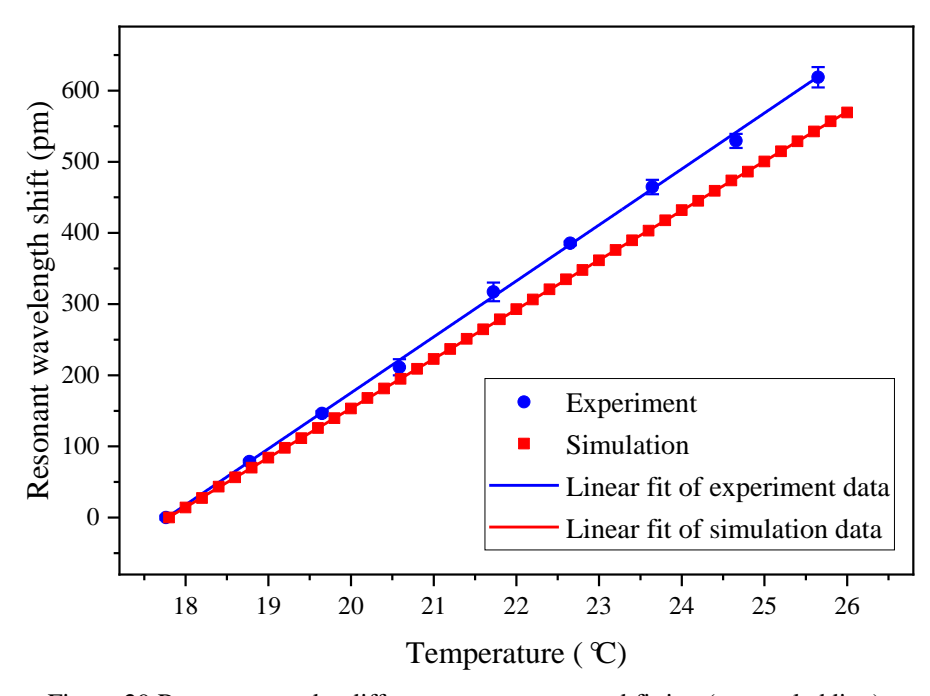


Figure 29 Resonance under different temperatures and fitting (water cladding)

Therefore, the detection sensitivity of the micro ring resonator is obtained, with a value of 78.64 pm/°C, representing that 1°C temperature change causes a shift in the resonant wavelength of 78.64 pm. The sensitivity value obtained by simulation is 69.46 pm/°C. The possible reasons for the difference between measurement and simulation include the differences on thermal-optical coefficients in simulation and test, the temperature difference between measured value and actual temperature of the waveguide and difference of waveguide dimensions caused by fabrication errors.

Then, the test of refractive index sensitivity of ring resonator was conducted by using sodium chloride aqueous solutions of different concentrations. Firstly, the chip was flushed by injecting deionized water in the microfluidic channel, and then a series of NaCl solutions with concentrations of 2.5%, 5%, 10%, 15% and 20% (mass concentrations) using deionized water were prepared and then injected into the microfluidic channel with a flow rate of 60µl/min. At the same time, the output transmission spectra of the microring resonator were recorded. The real-time resonance shift with changing of different concentrations NaCl solutions flowing over the microring resonator is shown in Figure 30. The response time during the measurements were around 100s, as shown in appendix. The transmission spectra with different concentrations sodium chloride aqueous solutions flowing over the resonator are shown in Figure 31.

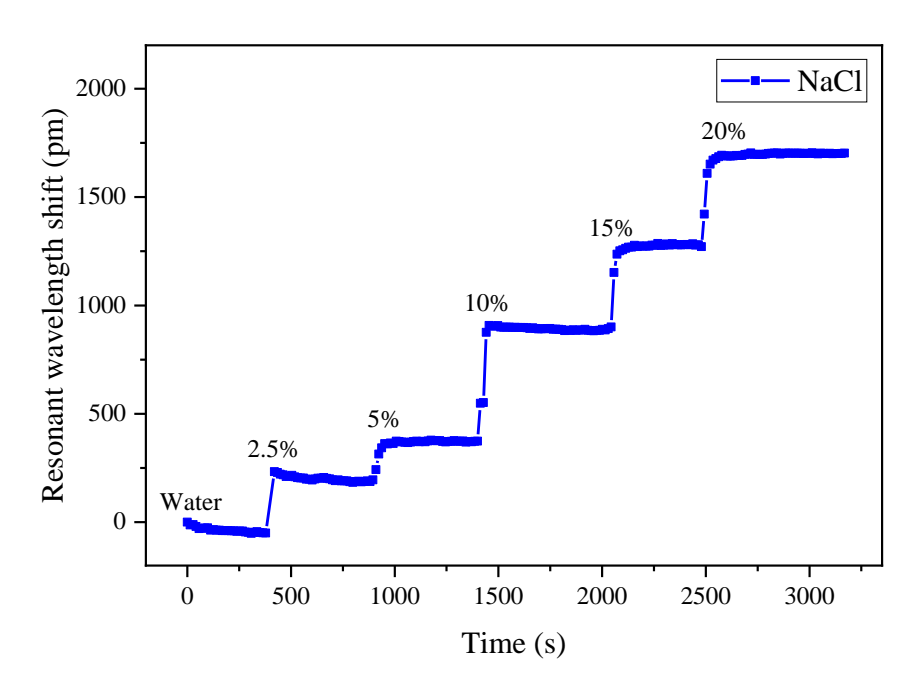


Figure 30 Real-time resonance shift with different concentrations NaCl solution flowing over the ring

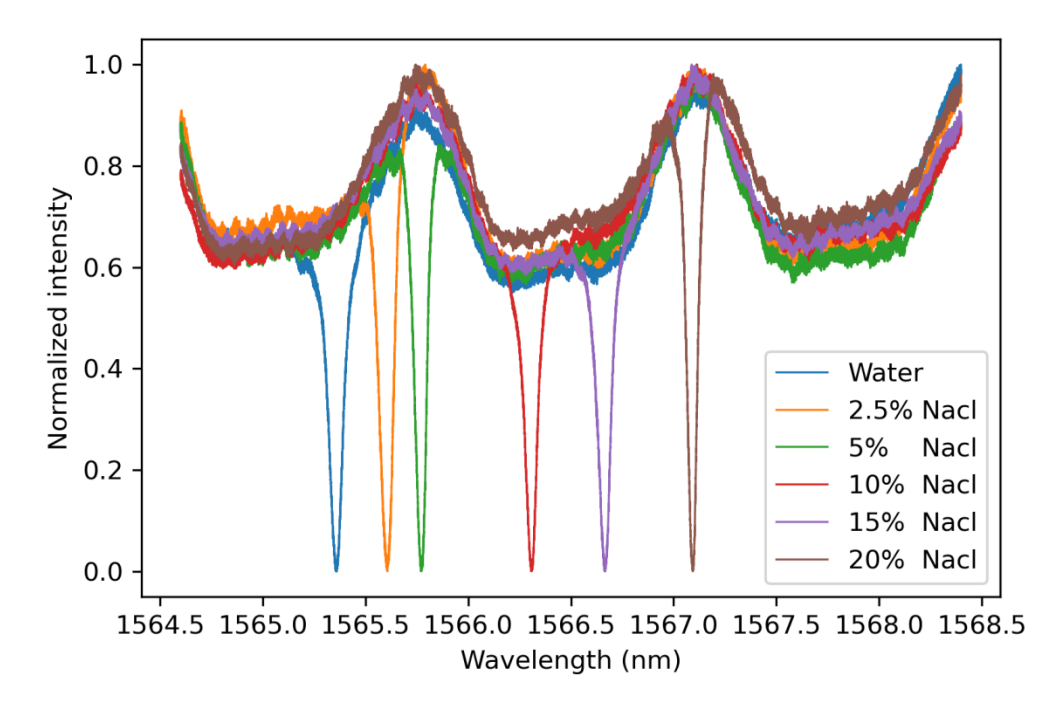


Figure 31 The spectra of microring resonances under different concentration NaCl solutions

From Figure 31, it can be seen that as the concentration of the solution increases, the resonant wavelength shifts towards the longer wavelength. The higher the concentration, the greater the resonance shifts. In order to calculate the detection sensitivity of the microring resonator, it is first necessary to obtain the refractive indexes of the solution with different concentrations, as listed in Table 4.

Table 4 Refractive indexes of sodium chloride solutions with different concentration [48]

Concentration (%)	2.5	5	10	15	20
Refractive index	1.3417	1.346	1.3544	1.3625	1.3703

The relationship between the change in the refractive index of the solution and the shift of the resonant wavelength is then obtained with a linear fitting:

$$\Delta \lambda = 53.30259n - 71.29787 \tag{26}$$

where is the resonant wavelength shift and n is the refractive index, with a coefficient of determination of 0.99794, indicating a good linearity.

Therefore, the detection sensitivity of the micro ring resonator is obtained, which is 53.30259 nm/RIU, indicating that a change in refractive index per unit can cause approximately a shift of 53 nm in the resonant wavelength. The minimum resolution of the wavelength at the output of the testing system is 0.2 pm, therefore, according to

Equation(18), the detection limit of the micro ring resonator is $0.0002/53.30259=3.752\times10^{-6}$ RIU. Therefore, under the current testing conditions, the micro ring resonator can detect a minimum change in refractive index of 3.752×10^{-6} RIU.

To verify the reliability of the test results of bulk refractive index sensing based on sodium chloride solutions, the similar tests based on glucose aqueous solutions were conducted. A series of glucose solutions with mass concentrations of 5%, 10%, 15%, and 20% were prepared using deionized water, and then injected into the microfluidic channel at a flow rate of $60 \,\mu\text{l/min}$, while measuring the output transmission spectra of the resonator. To prevent glucose molecules from condensing and adsorbing on the waveguide surface, deionized water was introduced to the microfluidic channel every time before the sample replacing to clean the sensing area.

The sensing results are shown in Figure 32 and corresponding optical transmission spectra are shown in Figure 33.

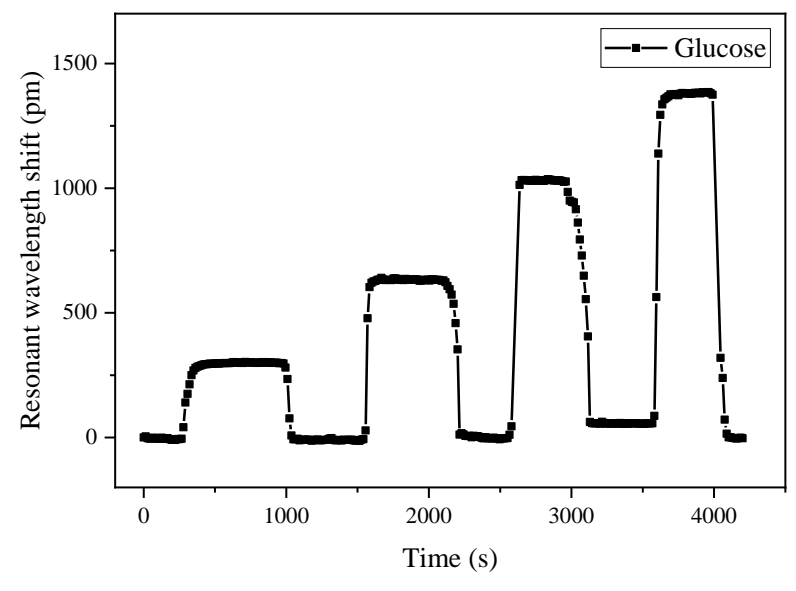


Figure 32 Resonance shift with different concentrations glucose solution flowing over the ring

Table 5 Refractive indexes of glucose solutions with different concentration[48]

Concentration (%)	5	10	15	20
Refractive index	1.34304	1.35003	1.35657	1.36267

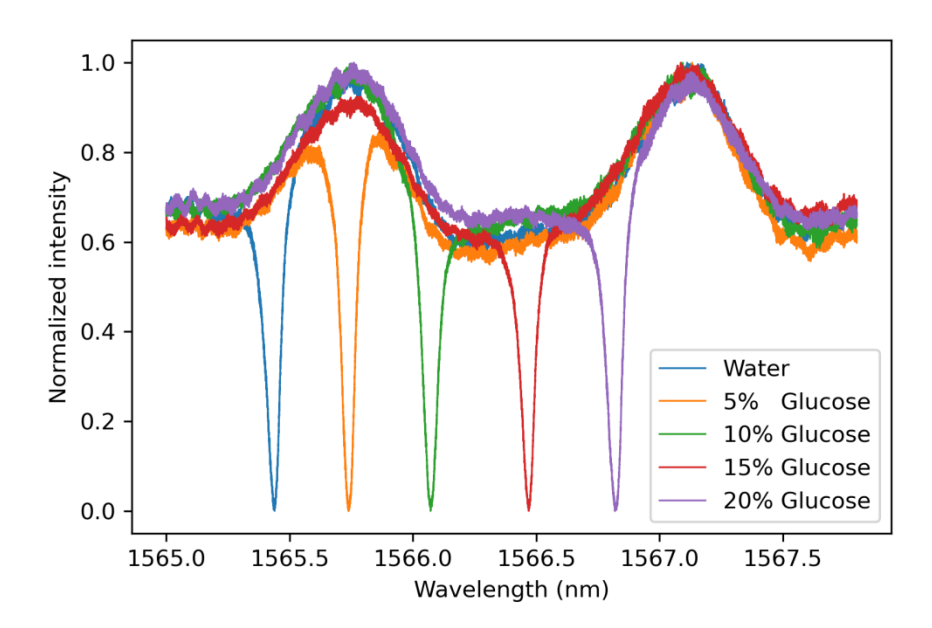


Figure 33 The spectra of microring resonances under different concentration glucose solutions Adopting the refractive indexes values in [48], as shown in Table 5, the resonance shift and refractive indexes are obtained, the relation can be expressed as

$$\Delta \lambda = 55.66676n - 74.48488 \tag{27}$$

The coefficient of determination is 0.99727, implying a good correlation and linearity. The detection limit of the micro ring resonator is 3.592×10^{-6} RIU. It can be seen that the relation obtained with glucose solutions is close to that obtained with sodium chloride solutions, which implies that the computed sensitivity and the limit of detection values are reliable. The data and linear fits obtained by both sodium chloride and glucose and the simulation results are shown in Figure 34.

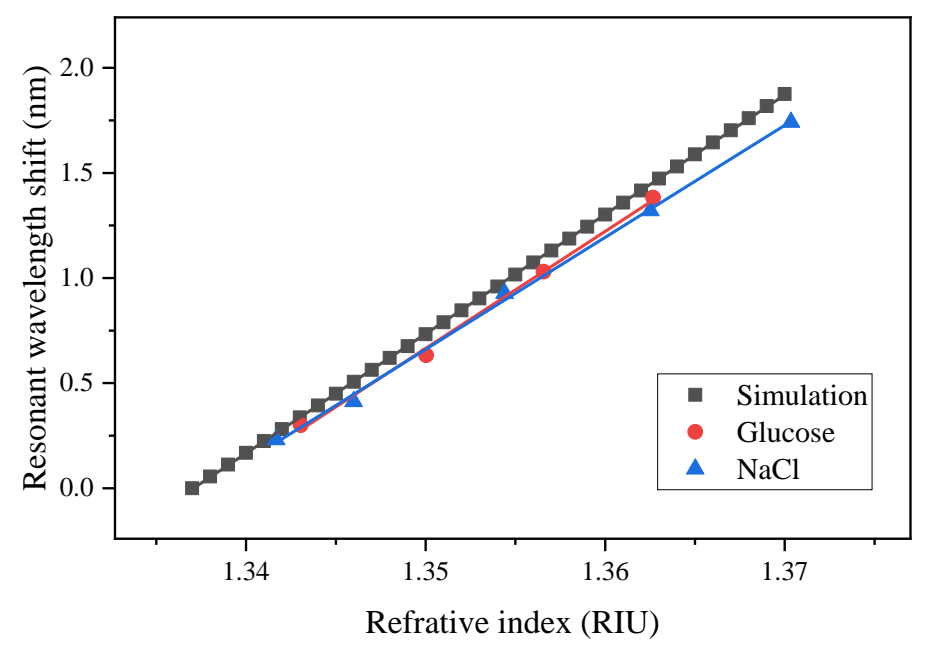


Figure 34 Resonant wavelengths with refractive index changes and their linear fits

The sensitivity computed from NaCl solution test results and glucose solution test results are 53.30 nm/RIU and 55.67 nm/RIU, respectively. These results show that the resonator has a good sensing performance and reproducibility. The sensitivity obtained by simulations is 56.82 nm/RIU, which is close to experimental results. The possible reasons for the difference between test results and simulations include the errors in refractive indices of test solutions, differences on actual refractive indices and that adopted in simulations, and difference of waveguide dimensions caused by fabrication errors.

4.2 Biosensing characterization

The biosensing characterization was conducted based on bulk sensing of whey protein solutions. Solutions for sensing were prepared with commercial whey protein powder (contains milk whey protein concentrate and emulsifiers) in mass concentrations of 0.5%, 1% and 3%. The optical transmission spectra were measured when water and different concentrations whey solutions flowed over the microring resonator. The test results are shown in Figure 35.

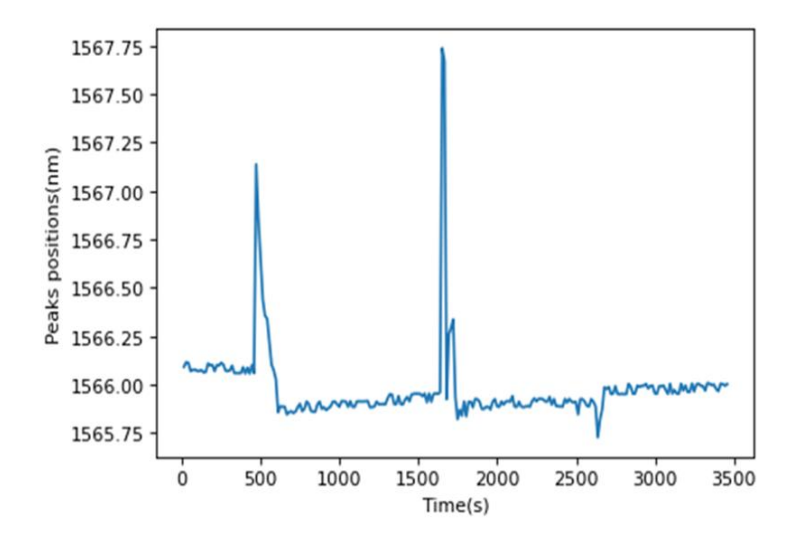


Figure 35 Real-time detection of peaks positions based on whey protein solution

It is observed that the resonant wavelength exhibited a shift to short wavelength direction when the whey solution flowed over the waveguide. And the higher the concentration, the larger the wavelength shift.

This test exhibited some differences compared with previous sensing test based on sodium chloride and glucose solution, the phenomena, possible explanations and potential solutions are as follows:

- (1) The 2 peaks were introduced by air bubbles caused by liquid switching, which can be solved by introducing a bubble trap in microfluidics system;
- (2) Larger fluctuations were observed. This might be because the solutions are less homogeneous;
- (3) The resonance blue-shifted might because the whey powder include other components, like fat, which influence the refractive index;
- (4) The peak position did not return to original value after flushing with water. This might be because whey powder includes other components which were attached on waveguide surface that were not able to flush away, as shown in Figure 36.

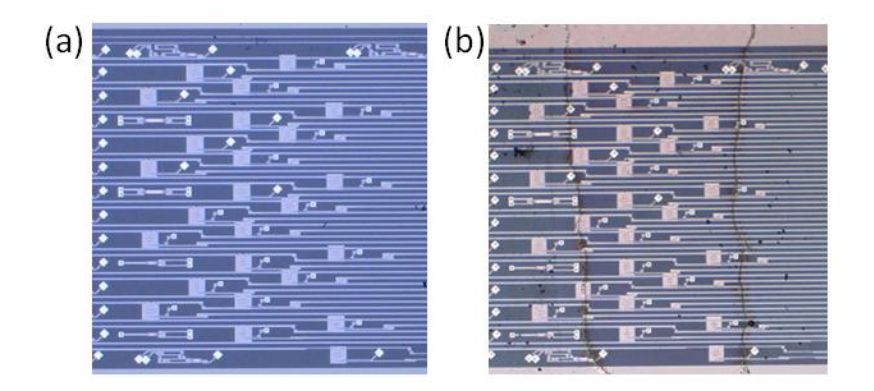


Figure 36 Image of the integrated photonics chip: (a) before test, (b) after test.

To investigate the phenomenon that test exhibited differences from sensing based on sodium chloride and glucose solutions, the tests were conducted based on centrifuged whey solutions. Centrifuge can separate the water-insoluble particles from the solution and therefore solutions contain water-soluble proteins were obtained. The tests were conducted based on centrifuged whey solutions with mass concentrations of 0.5%, 1%, 2% and 3%. Deionized water was adopted to clean the sensing area every time before the sample replacing. One resonant peak was selected from the transmission spectrum and the position of the peak was traced in real-time measurements. The test results are shown in Figure 37. The resonant wavelength exhibited red-shifts with the increase of solution concentration. However, different from the tests based on sodium chloride and glucose solutions, resonant wavelength did not return the original value after flushing, indicating that some particles were attached to the waveguide.

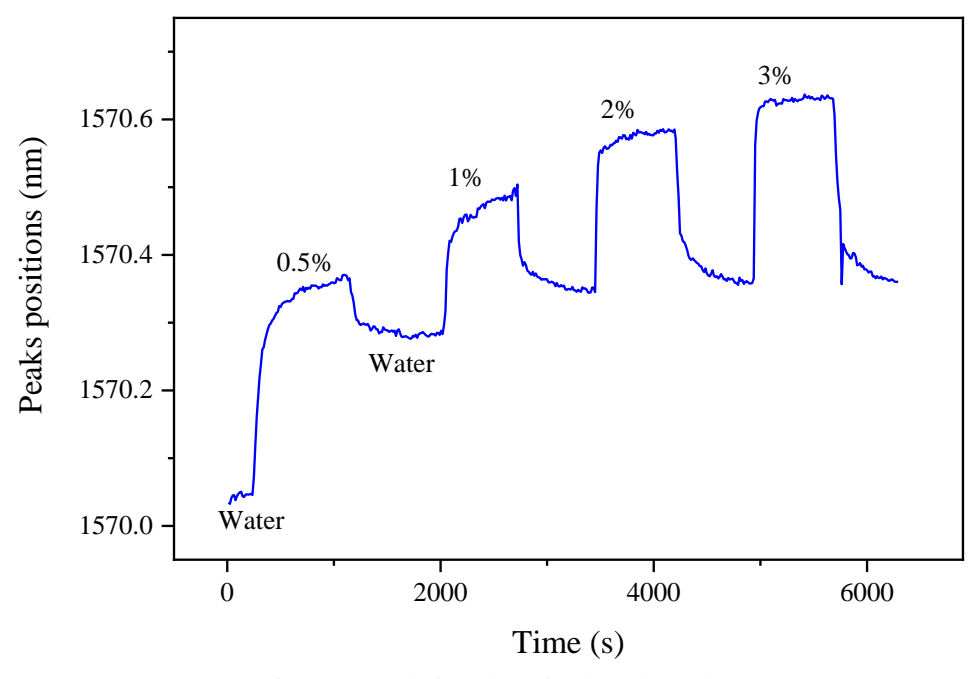


Figure 37 Real-time detection based on whey

The resonance positions on the spectra under different concentrations of solutions were obtained, as shown in Figure 38. As the increase of the concentration, the peak position exhibited a red shift.

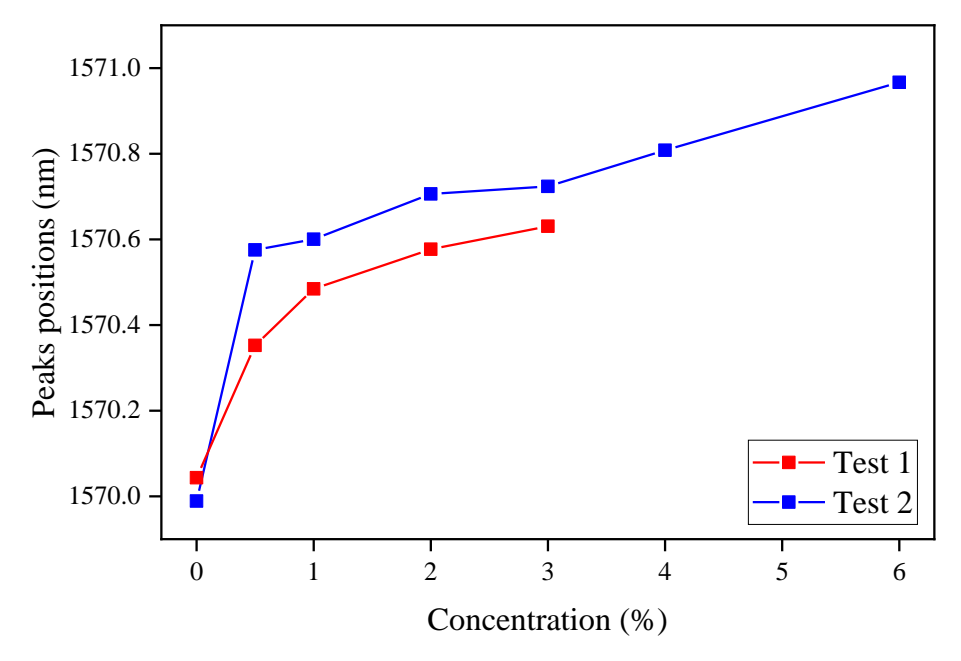


Figure 38 Wavelength shift under different concentrations

Since the resonant wavelength after flushing did not back to the initial value, to investigate this phenomenon, wavelength shift after each flush relative to initial and

relative to last flush were computed, as shown in Figure 39. The wavelength shift after each flush relative to initial value increased as the increase of concentration, until saturation was reached. The wavelength shift relative to last flush first exhibited a large change, and then gradually increases with the increase of concentration. The possible reason is that at the starting phase the particles were attached to the waveguide while the cladding refractive index was changing, however, after the particle attachment reached saturation the change of wavelength was contributed by only the cladding refractive index change.

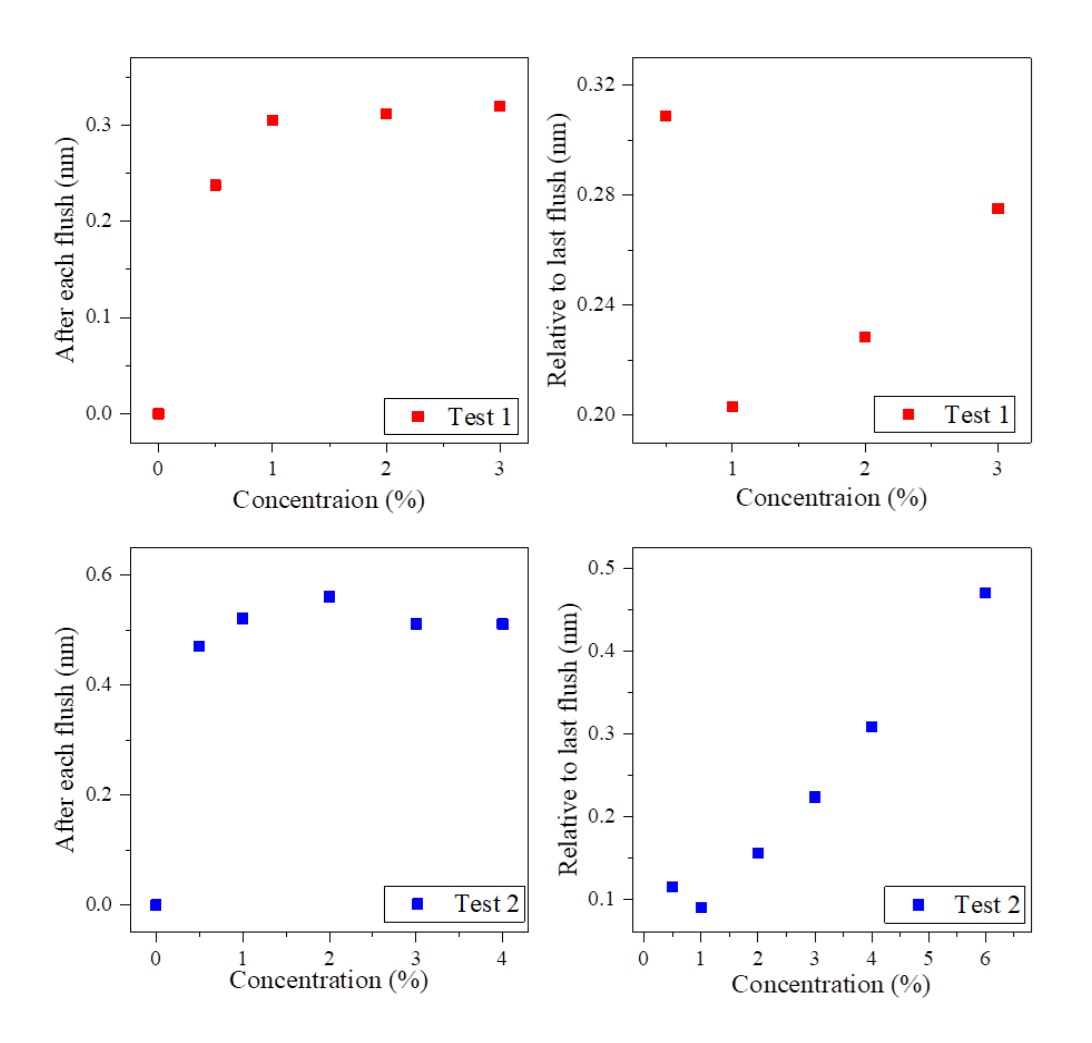


Figure 39 Resonant wavelength shift after each flush relative to initial and relative to last flush

4.3 Summary and discussions

The sensing based on microring resonator was investigated and the feasibility and effectiveness of the optical waveguide chip sensing was verified.

The results confirmed that the microring resonator has a good performance for

sensing with sufficient sensitivity (53 nm/RIU) and detection limit (3.75×10⁻⁶ RIU), which are comparable to the results by Salleh et al. [30](12.7 nm/RIU) and Wu et al. [28] (5.708×10⁻⁵ RIU and 140 nm/RIU). The data demonstrated a reasonable relation between the microfluidics environment change of ring resonator and the resonant wavelength, which aligns with prior studies [25, 28, 30]. Furthermore, sensing with complex component aqueous protein solutions were investigated, which explored the possibility to sense solutions with complex components by volume sensing with microring resonator. Although the results were not able to be formulated, they still show some noteworthy patterns.

Nevertheless, the study has several limitations. Because of time limit, the sensing with waveguide surface functionalization was not conducted. Secondly, the sensor requires complex test setup, which is a barrier to portable practical applications. The pump-free microfluidic integrated chip should be designed for practical applications. Additionally, the resonator is sensitive to large particle contaminations, and therefore how to prevent large particles influencing the sensing results and sensing performance should be considered.

In conclusion, this study investigated the sensing of microring resonator with microfluidics and preliminarily verified the possibility of photonic microring resonator for biosensing. By addressing the limitations and building upon the results, future studies can investigate the biosensing with chemical receptors on waveguide.

5 Conclusions and outlook

This thesis analyzed the working principle, research progress, and application of microring resonator biosensing system. The microfluidic channel was designed and integrated to the microring resonator. And real-time detection was carried out using this sensing system. The main work and conclusions are as follows:

The sensitivities and the optical read-out changes under different sensing conditions (surface biosensing, bulk refractive index sensing and temperature sensing) were simulated in software RSoft, which concludes that there is a linear relation between resonant wavelength shift and the sensing parameters, and the sensitivities are detectable.

The multiphysics finite element analysis was employed to simulate the bio-analyte transportation and adsorption in microfluidic channel, so as to design and optimize the microfluidic channel. For a microring with radius of $14 \, \mu m$ uniform biomarker binding requires at least a channel with width $175 \, \mu m$ and height $70 \, \mu m$. The microfluidic channel were fabricated and further integrated to the photonics chip, providing a stable fluid environment for conducting measurements.

A series of tests were conducted on SOI microring resonator. The thermal sensitivity was measured, with a value of 78.64 pm/°C. Homogeneous sensing was performed using NaCl and glucose solutions of different concentrations. The refractive index sensitivity was measured to be 53 nm/RIU, and homogeneous sensing was tested for different protein solutions.

The future works might include:

Test the resonator with functionalized biosensing layer.

Design micro ring resonators array for parallel measurement. Adopt precision dispensing or multi-channel microfluidic chip to functionalize the resonators, so as to achieve multi-analyte detection with single test.

This thesis used external light source and detector, which require a very stable testing environment. In the future, integrating the light sources and detectors with sensors on a single chip will further achieve the goal of portability and miniaturization of the sensor.

References

- [1] I.-H. Cho, D. H. Kim, and S. Park, "Electrochemical biosensors: perspective on functional nanomaterials for on-site analysis," *Biomaterials Research*, vol. 24, no. 1, p. 6, 2020/02/04 2020.
- [2] L. Wang *et al.*, "Rapid and ultrasensitive electromechanical detection of ions, biomolecules and SARS-CoV-2 RNA in unamplified samples," *Nature Biomedical Engineering*, vol. 6, no. 3, pp. 276-285, 2022/03/01 2022.
- [3] V. R. Samuel and K. J. Rao, "A review on label free biosensors," *Biosensors and Bioelectronics:* X, vol. 11, 2022.
- [4] P. Steglich, M. Hulsemann, B. Dietzel, and A. Mai, "Optical Biosensors Based on Silicon-On-Insulator Ring Resonators: A Review," *Molecules*, vol. 24, no. 3, Jan 31 2019.
- [5] X. Fan, I. M. White, S. I. Shopova, H. Zhu, J. D. Suter, and Y. Sun, "Sensitive optical biosensors for unlabeled targets: A review," *Analytica Chimica Acta*, vol. 620, no. 1, pp. 8-26, 2008/07/14/2008.
- [6] E. Luan, H. Shoman, D. M. Ratner, K. C. Cheung, and L. Chrostowski, "Silicon Photonic Biosensors Using Label-Free Detection," *Sensors (Basel)*, vol. 18, no. 10, Oct 18 2018.
- [7] R. Peltomaa, B. Glahn-Martínez, E. Benito-Peña, and M. C. Moreno-Bondi, "Optical Biosensors for Label-Free Detection of Small Molecules," (in eng), *Sensors (Basel)*, vol. 18, no. 12, Nov 24 2018.
- [8] Y. R. Bawankar and A. Singh, "Microring Resonators Based Applications in Silicon Photonics A Review," in *2021 5th Conference on Information and Communication Technology (CICT)*, 2021, pp. 1-6.
- [9] N. L. Kazanskiy, S. N. Khonina, and M. A. Butt, "A Review of Photonic Sensors Based on Ring Resonator Structures: Three Widely Used Platforms and Implications of Sensing Applications," vol. 14, no. 5, p. 1080, 2023.
- [10] D. Martens and P. Bienstman, "Study on the limit of detection in MZI-based biosensor systems," *Sci Rep*, vol. 9, no. 1, p. 5767, Apr 8 2019.
- [11] P. P. Vachali, B. Li, A. Bartschi, and P. S. Bernstein, "Surface plasmon resonance (SPR)-based biosensor technology for the quantitative characterization of protein-carotenoid interactions," *Arch Biochem Biophys*, vol. 572, pp. 66-72, Apr 15 2015.
- [12] M. C. Estevez, M. Alvarez, and L. M. Lechuga, "Integrated optical devices for lab-on-a-chip biosensing applications," *Laser & Photonics Reviews*, vol. 6, no. 4, pp. 463-487, 2012.
- [13] Y.-S. Sun and X. Zhu, "Kinetic Analysis of Biomolecular Interactions Using Label-Free Biosensors," *Instrumentation Science & Technology*, vol. 43, 02/28 2015.
- [14] J. Hu *et al.*, "Low-loss high-index-contrast planar waveguides with graded-index cladding layers," *Optics Express*, vol. 15, no. 22, pp. 14566-14572, 2007/10/29 2007.
- [15] P. K. Chatterjee *et al.*, "20 Integrated Circuits," in *Reference Data for Engineers (Ninth Edition)*, W. M. Middleton and M. E. Van Valkenburg, Eds. Woburn: Newnes, 2002, pp. 20-1-20-113.
- [16] K. Yamada, "Silicon Photonic Wire Waveguides: Fundamentals and Applications," vol. 119, 1970, pp. 1-29.
- [17] A. Mattheyses and D. Axelrod, "Direct measurement of the evanescent field profile produced

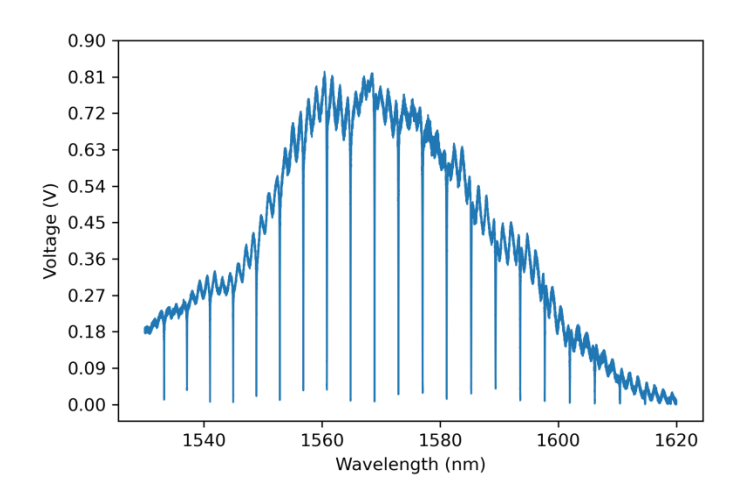
- by objective-based total internal reflection fluorescence," *Journal of Biomedical Optics,* vol. 11, no. 1, p. 014006, 2006.
- [18] L. F. Kui and M. R. Uddin, "Photonic microring resonator modulated resonance response analysis," *Optical and Quantum Electronics*, vol. 49, no. 8, p. 275, 2017/07/24 2017.
- [19] X. Han *et al.*, "Quasi-single-sideband radio over fiber transmission with a polymer-based waveguide microring resonator," vol. 50, no. 12, pp. 124601-124601-7, 2011.
- [20] M. Soler and L. M. Lechuga, "Biochemistry strategies for label-free optical sensor biofunctionalization: advances towards real applicability," *Anal Bioanal Chem,* vol. 414, no. 18, pp. 5071-5085, Jul 2022.
- [21] C. Adamopoulos, A. Gharia, A. Niknejad, V. Stojanovic, and M. Anwar, "Microfluidic Packaging Integration with Electronic-Photonic Biosensors Using 3D Printed Transfer Molding," *Biosensors (Basel)*, vol. 10, no. 11, Nov 14 2020.
- [22] A. G. Niculescu, C. Chircov, A. C. Birca, and A. M. Grumezescu, "Fabrication and Applications of Microfluidic Devices: A Review," *Int J Mol Sci*, vol. 22, no. 4, Feb 18 2021.
- [23] C. Szydzik *et al.*, "An automated optofluidic biosensor platform combining interferometric sensors and injection moulded microfluidics," *Lab Chip*, vol. 17, no. 16, pp. 2793-2804, Aug 8 2017.
- [24] Z. Wang *et al.*, "Microfluidic channels with ultralow-loss waveguide crossings for various chip-integrated photonic sensors," *Opt Lett*, vol. 40, no. 7, pp. 1563-6, Apr 1 2015.
- [25] C. F. Carlborg *et al.*, "A packaged optical slot-waveguide ring resonator sensor array for multiplex label-free assays in labs-on-chips," *Lab Chip*, vol. 10, no. 3, pp. 281-90, Feb 7 2010.
- [26] A. L. Washburn, J. Gomez, and R. C. Bailey, "DNA-encoding to improve performance and allow parallel evaluation of the binding characteristics of multiple antibodies in a surface-bound immunoassay format," *Anal Chem,* vol. 83, no. 9, pp. 3572-80, May 1 2011.
- [27] R. Heideman, M. Hoekman, and E. Schreuder, "TriPleX-Based Integrated Optical Ring Resonators for Lab-on-a-Chip and Environmental Detection," *IEEE Journal of Selected Topics in Quantum Electronics*, vol. 18, no. 5, pp. 1583-1596, 2012.
- [28] S. Wu, Y. Guo, W. Wang, J. Zhou, and Q. Zhang, "Label-free biosensing using a microring resonator integrated with poly-(dimethylsiloxane) microfluidic channels," *Rev Sci Instrum*, vol. 90, no. 3, p. 035004, Mar 2019.
- [29] C. J. Choi, I. D. Block, B. Bole, D. Dralle, and B. T. Cunningham, "Label-Free Photonic Crystal Biosensor Integrated Microfluidic Chip for Determination of Kinetic Reaction Rate Constants," *IEEE Sensors Journal*, vol. 9, no. 12, pp. 1697-1704, 2009.
- [30] M. H. M. Salleh, A. Glidle, M. Sorel, J. Reboud, and J. M. Cooper, "Polymer dual ring resonators for label-free optical biosensing using microfluidics," *Chemical Communications*, 10.1039/C3CC38228A vol. 49, no. 30, pp. 3095-3097, 2013.
- [31] K. De Vos, I. Bartolozzi, E. Schacht, P. Bienstman, and R. J. O. e. Baets, "Silicon-on-Insulator microring resonator for sensitive and label-free biosensing," vol. 15, no. 12, pp. 7610-7615, 2007.
- [32] M. Fukuyama *et al.*, "Detection of antigen–antibody reaction using Si ring optical resonators functionalized with an immobilized antibody-binding protein," vol. 50, no. 4S, p. 04DL07, 2011.
- [33] G. Gaur, S. Hu, R. L. Mernaugh, I. I. Kravchenko, S. T. Retterer, and S. M. Weiss, "Label-free detection of Herceptin® using suspended silicon microring resonators," *Sensors and*

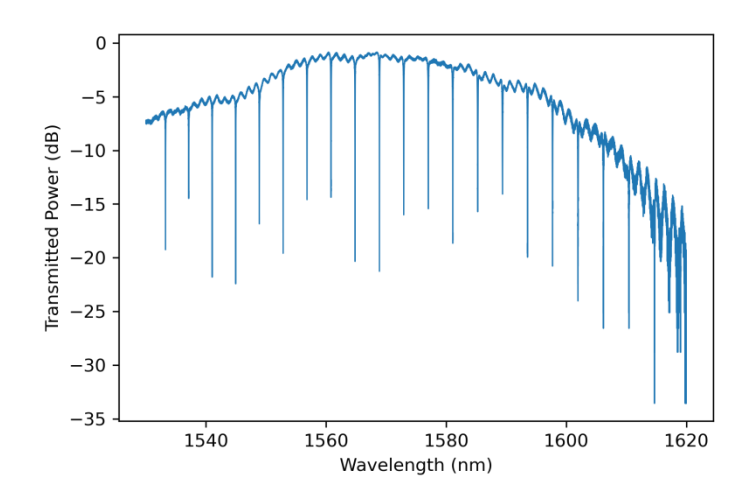
- Actuators B: Chemical, vol. 275, pp. 394-401, 2018/12/01/ 2018.
- [34] O. Scheler *et al.*, "Label-free, multiplexed detection of bacterial tmRNA using silicon photonic microring resonators," *Biosensors and Bioelectronics*, vol. 36, no. 1, pp. 56-61, 2012/06/01/2012
- [35] Y. Chen *et al.*, "Label-free biosensing using cascaded double-microring resonators integrated with microfluidic channels," *Optics Communications*, vol. 344, pp. 129-133, 2015.
- [36] W. J. Westerveld and H. P. Urbach, Silicon Photonics: IOP Publishing, 2017. [Online]. Available: https://dx.doi.org/10.1088/978-0-7503-1386-5.
- [37] H. Nejadriahi, A. Friedman, R. Sharma, S. Pappert, Y. Fainman, and P. Yu, "Thermo-optic properties of silicon-rich silicon nitride for on-chip applications," *Optics Express*, vol. 28, no. 17, pp. 24951-24960, 2020/08/17 2020.
- [38] Y. Okada and Y. Tokumaru, "Precise determination of lattice parameter and thermal expansion coefficient of silicon between 300 and 1500 K," *Journal of Applied Physics*, vol. 56, no. 2, pp. 314-320, 1984.
- [39] C.-K. Yang, J.-S. Chang, S. D. Chao, and K.-C. Wu, "Effects of diffusion boundary layer on reaction kinetics of immunoassay in a biosensor," *Journal of Applied Physics*, vol. 103, no. 8, 2008
- [40] J. A. Capobianco, W. Y. Shih, G. P. Adams, and W.-H. Shih, "Label-free Her2 detection and dissociation constant assessment in diluted human serum using a longitudinal extension mode of a piezoelectric microcantilever sensor," *Sensors and Actuators B: Chemical*, vol. 160, no. 1, pp. 349-356, 2011/12/15/2011.
- [41] C. F. Huang *et al.*, "Analysis for Replication and Surface Roughness of Micro-Feature of Silicon Mold Insert by UV-LIGA Method," *Advanced Materials Research*, vol. 47-50, pp. 443-446, 2008.
- [42] J. C. Love, D. B. Wolfe, H. O. Jacobs, and G. M. Whitesides, "Microscope Projection Photolithography for Rapid Prototyping of Masters with Micron-Scale Features for Use in Soft Lithography," *Langmuir*, vol. 17, no. 19, pp. 6005-6012, 2001/09/01 2001.
- [43] C. Luo, F. Meng, and A. Francis, "Fabrication and application of silicon-reinforced PDMS masters," *Microelectronics Journal*, vol. 37, pp. 1036-1046, 10/01 2006.
- [44] T. Scharnweber, R. Truckenmüller, A. M. Schneider, A. Welle, M. Reinhardt, and S. Giselbrecht, "Rapid prototyping of microstructures in polydimethylsiloxane (PDMS) by direct UV-lithography," *Lab on a Chip,* 10.1039/C0LC00567C vol. 11, no. 7, pp. 1368-1371, 2011.
- [45] B. Venzac *et al.*, "PDMS Curing Inhibition on 3D-Printed Molds: Why? Also, How to Avoid It?," *Anal Chem*, vol. 93, no. 19, pp. 7180-7187, May 18 2021.
- [46] G. Comina, A. Suska, and D. Filippini, "PDMS lab-on-a-chip fabrication using 3D printed templates," *Lab Chip*, vol. 14, no. 2, pp. 424-30, Jan 21 2014.
- [47] P. H. King, G. Jones, H. Morgan, M. R. de Planque, and K. P. Zauner, "Interdroplet bilayer arrays in millifluidic droplet traps from 3D-printed moulds," *Lab Chip*, vol. 14, no. 4, pp. 722-9, Feb 21 2014.
- [48] C.-Y. Tan and Y.-X. Huang, "Dependence of Refractive Index on Concentration and Temperature in Electrolyte Solution, Polar Solution, Nonpolar Solution, and Protein Solution," *Journal of Chemical & Engineering Data*, vol. 60, no. 10, pp. 2827-2833, 2015/10/08 2015.

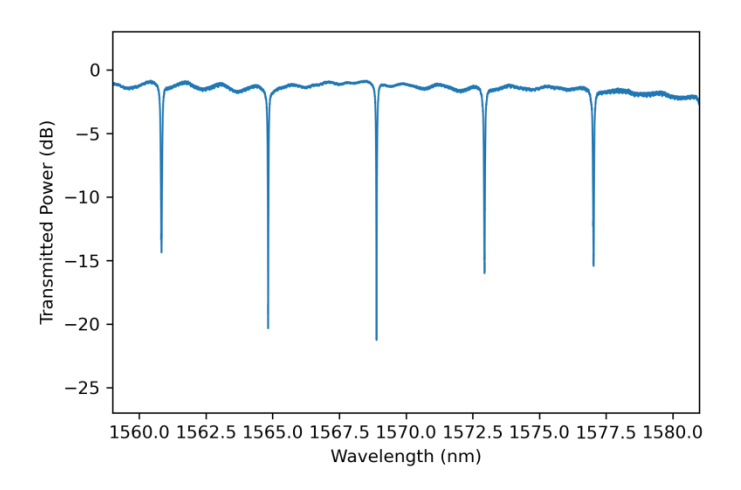
Appendix

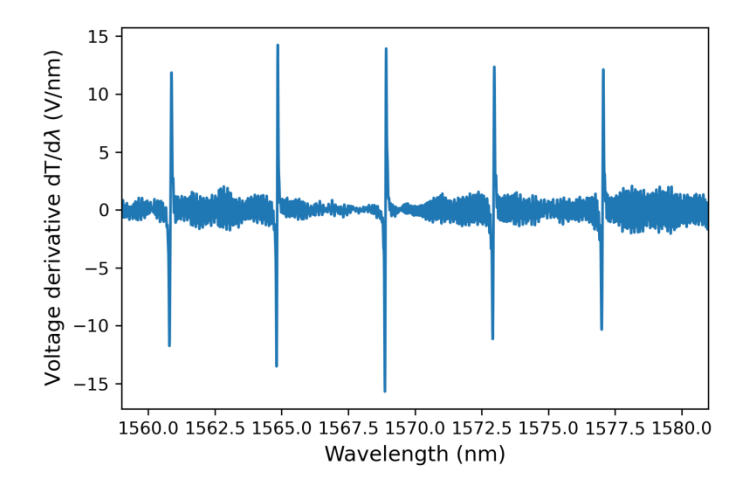
Extra characterization data:

Resonator performance under air cladding:

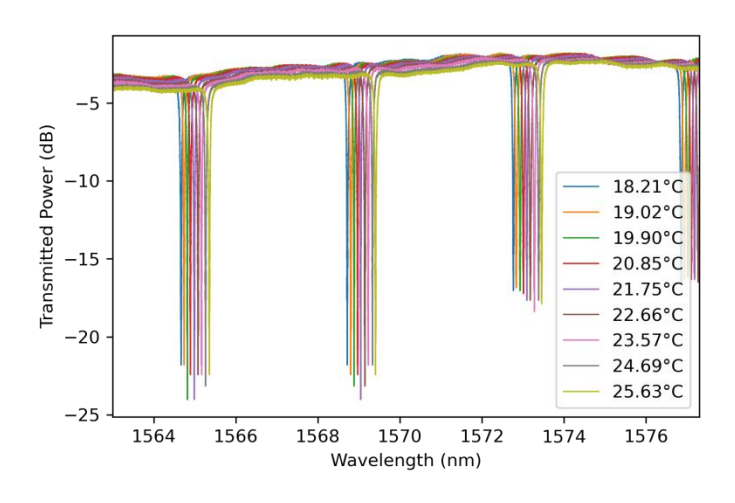


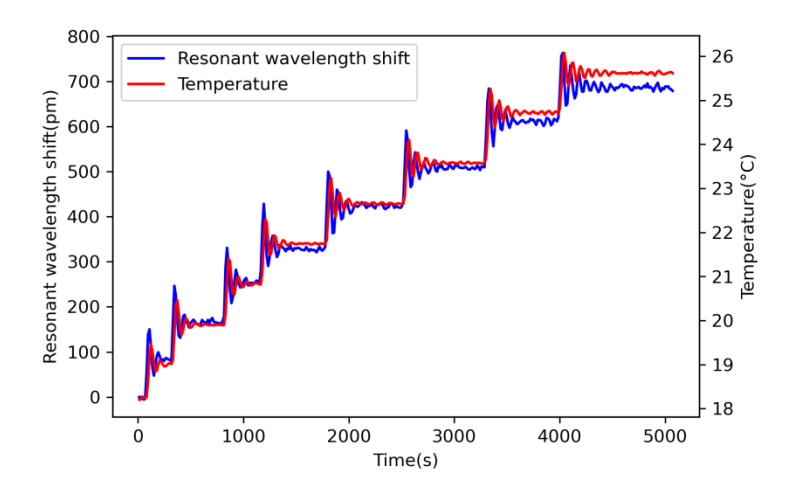


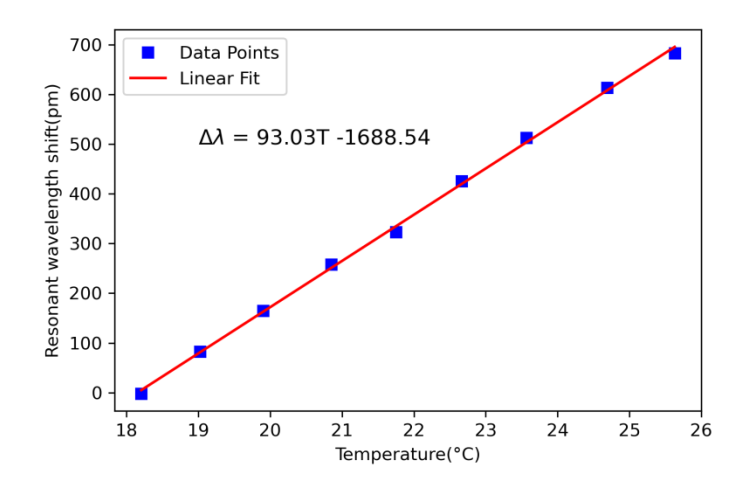


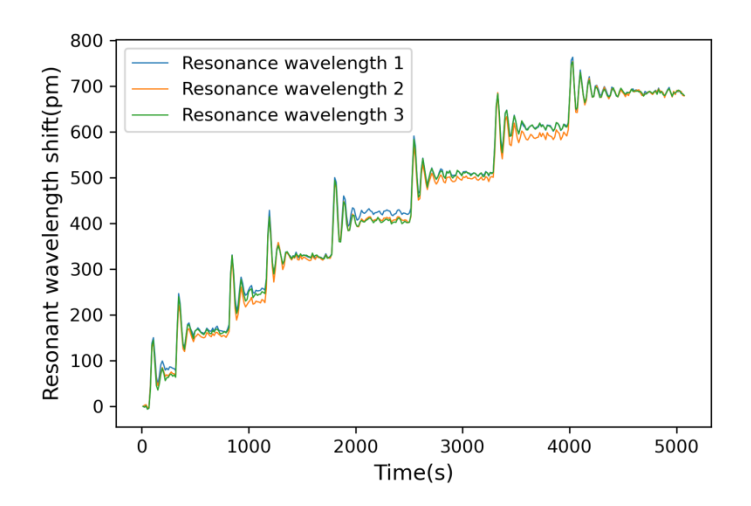


Temperature characterization under air cladding:



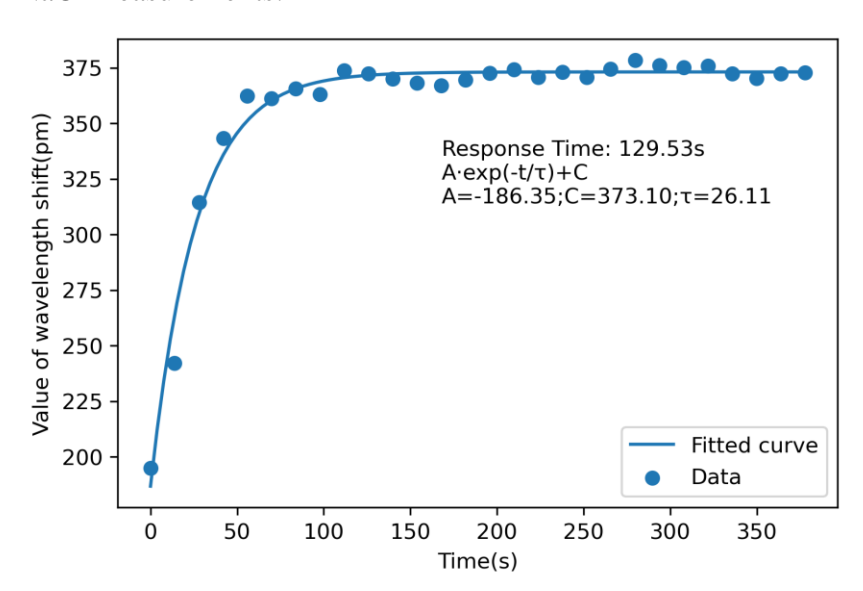


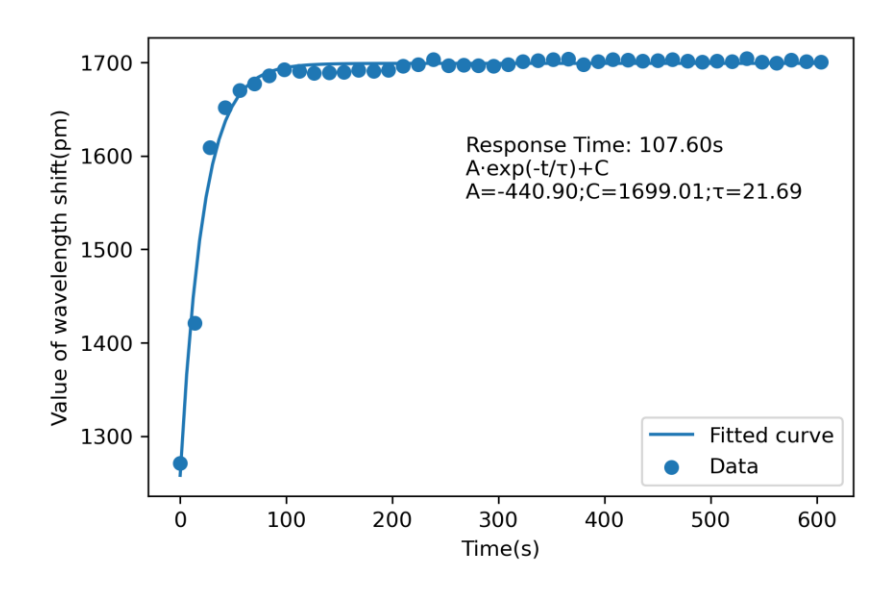


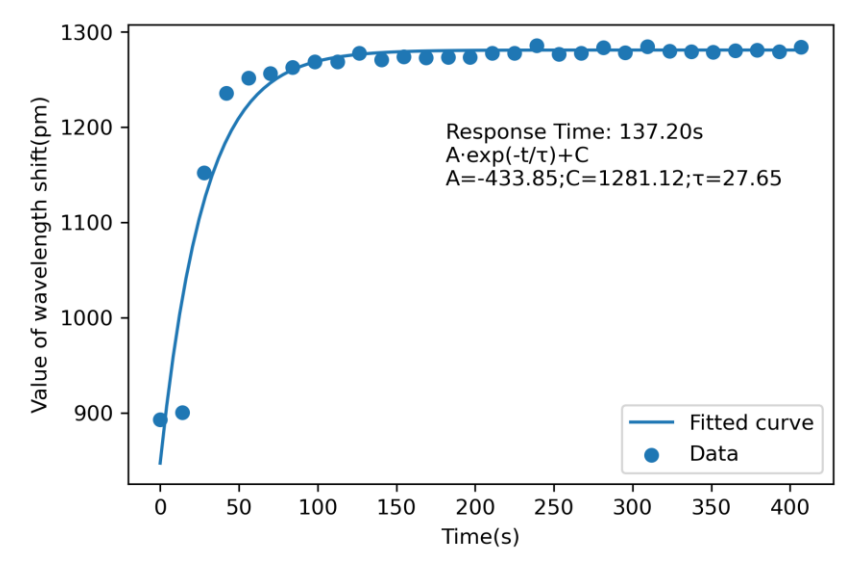


Response time during measurements:

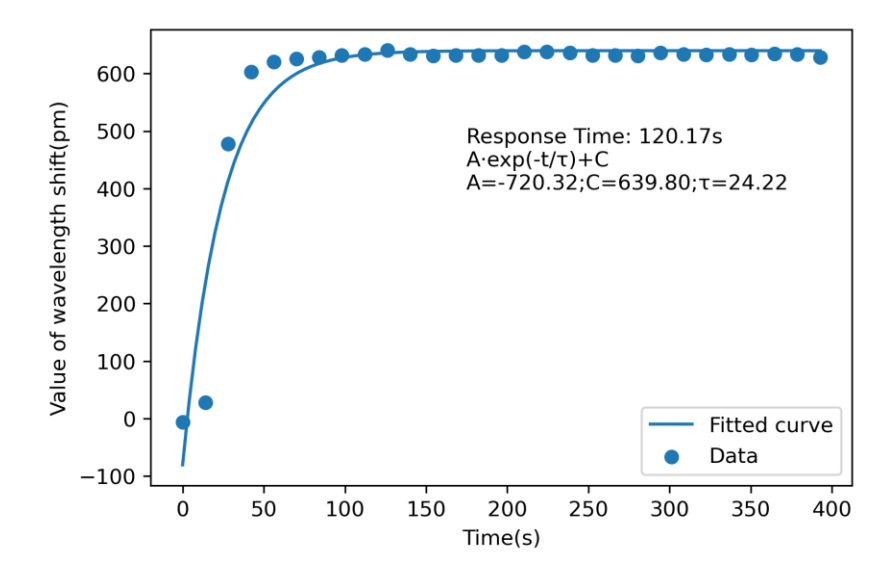
NaCl measurements:

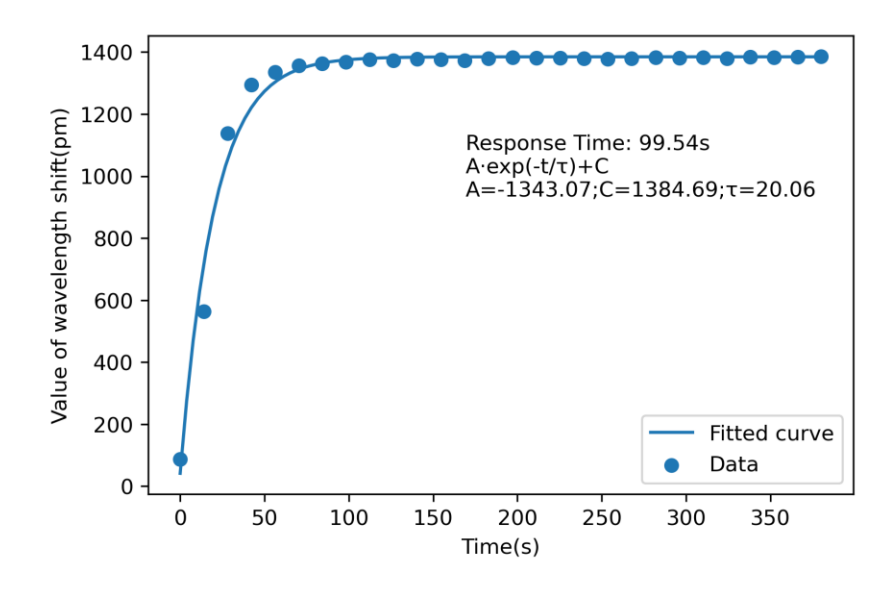


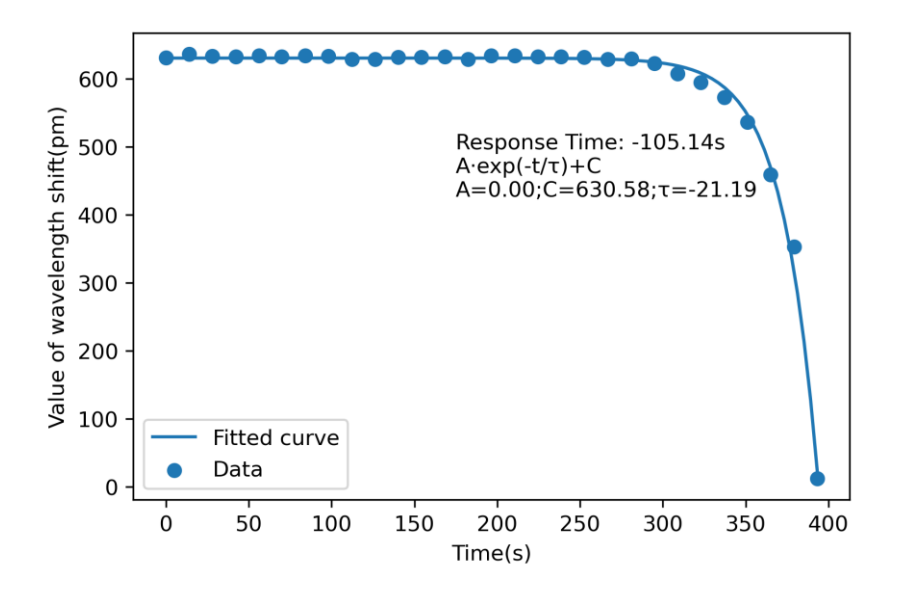




Glucose measurements:

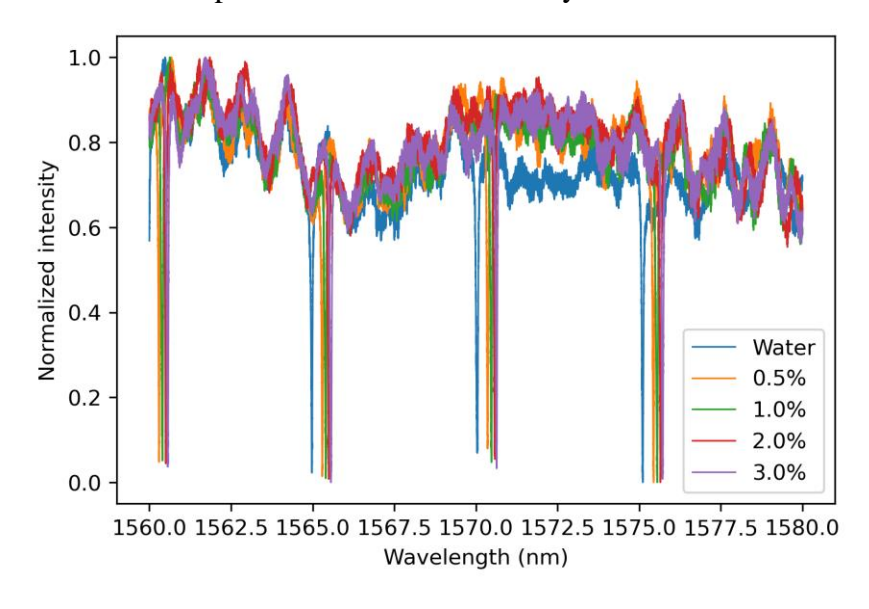


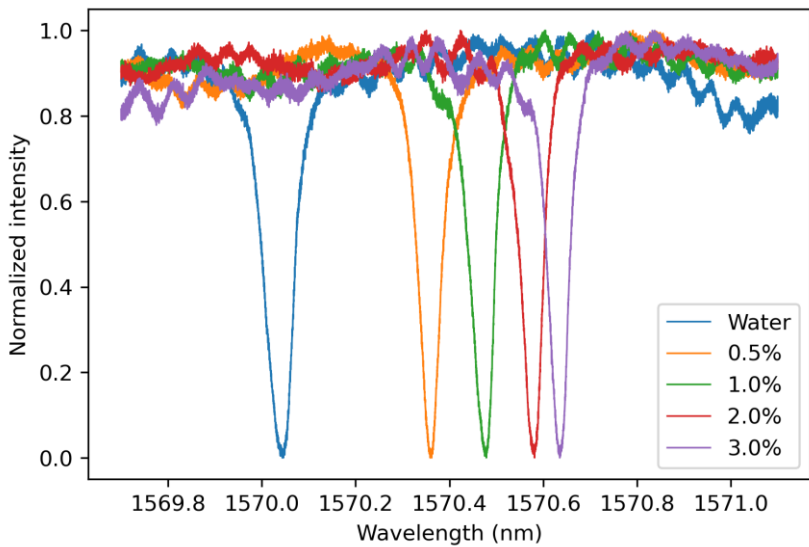




All the response times were computed as the settling time under 99.3% of its maximum value (1 - 1/e)

Transmission spectra of test based on whey solutions:





Extra measurement based on whey solutions:

